SPACE DOMAIN AWARENESS USING HIGH FREQUENCY LINE OF SIGHT AND IONOSPHERIC CORRECTION METHODS

LA VEILLE SPATIALE À L'AIDE DE MÉTHODES LIGNE DE MIRE À HAUTE FRÉQUENCE ET DE CORRECTION IONOSPHÉRIQUE

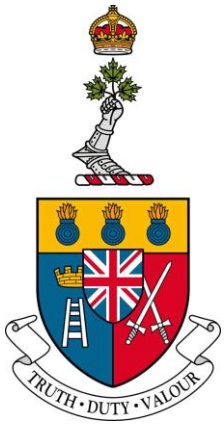

A Master Thesis Submitted
To the Department of Computer and Electrical Engineering
By

Kyra A. Czarnowske
Major

In partial Fulfillment of the Requirements for the Degree of
Master of Applied Science in Electrical Engineering

29 June 2023

Abstract

Space has become an increasingly active operational domain for both the private and public sectors. It is vital that the Department of National Defence (DND) has an accurate means to maintain visibility and control over their deployed space assets, as well as surrounding threats. Space Domain Awareness (SDA) is a concept that refers to the surveillance and tracking of deployed space assets and other objects to ensure operational security. Current methods of SDA include the use of ground and spaceborne optical telescopes, as well as radars operating in the upper frequency bands. Two Line Element sets (TLEs) are the most accessible means of orbital data and provide orbital position predictions with an accuracy of up to 1 km in position and 1 m/s in velocity. The growing popularity of smaller spacecrafts, such as CubeSats and micro-satellites, as an economical means to conduct space operations, has increased the need for more accurate SDA. This thesis tested the feasibility of using High Frequency (HF) radar to achieve accurate range and radial velocity estimations using Line of Sight (LoS) propagation and target detection. The International Space Station (ISS) was selected as the target, due to its large size and lower orbiting altitude. The operating frequency of 20 MHz was used to pierce the ionosphere and illuminate the selected target. Range-Doppler maps were produced with collected measurements, and corrections were applied to compensate for atmospheric and filter errors. The range errors were calculated using the Total Electron Content (TEC) estimations from Australian open-source software Provision of High-Frequency Raytracing Laboratory for Propagation Studies (PHaRLAP). The effect of the ionosphere at different levels of solar activity were compared via a night transmission period and a day transmission period. It was found that the night-time transmissions had overestimated TECs and corrections were not required, whereas the day-time transmissions measurements were found to be greatly affected by the larger TECs. The day-time transmissions produced estimated ionospheric range delays of up to 90 km and Doppler corrections up to 45 Hz. The night-time transmissions had average delays of 30 km and Doppler corrections of a maximum 15 Hz. The final range measurements after corrections had a Root Mean Square Error (RMSE) of 61 km over a 100 second period of visibility during day transmission and 28 km over a 450 second period during the night transmission. With such high range residuals, it was found that HF is unsuitable for accurate range measurements unless better ionospheric correction methods are developed and more intensive signal processing techniques are applied. However, the Doppler measurements for both the night and day transmission produced residual RMSE of less than 10 Hz. The night transmission range rate residuals had a RMSE of only 85 m/s, which is within the margin of error of the TLE accuracy. This suggests that HF can be used for accurate orbit determination using Doppler measurements.

Résumé

L'espace est devenu un domaine opérationnel de plus en plus actif pour les secteurs privé et public. Il est essentiel que le Ministère de la Défense Nationale (MDN) dispose de moyens précis pour maintenir la visibilité et le contrôle de ses ressources spatiales déployées, ainsi que des menaces environnantes. La veille spatiale (SDA) est un concept qui fait référence à la surveillance et au suivi des actifs spatiaux déployés et d'autres objets pour assurer la sécurité opérationnelle. Les méthodes actuelles de SDA comprennent l'utilisation de télescopes optiques terrestres et spatiaux, ainsi que de radars fonctionnant dans les bandes de fréquences supérieures. Les paramètres orbitaux à deux lignes (TLE) sont les moyens les plus accessibles de données orbitales et fournissent des prévisions de position avec une précision allant jusqu'à 1 km en position et 1 m/s en vitesse. La popularité croissante des engins spatiaux plus petits, tels que les CubeSats et les micro-satellites, en tant que moyen économique de mener des opérations spatiales, a augmenté le besoin d'une SDA plus précise. Cette thèse a testé la faisabilité d'utiliser des transmissions radar haute fréquence (HF) pour obtenir des estimations orbitales précises en utilisant la propagation en ligne de mire (LoS) et la détection de cible. La Station Spatiale Internationale (ISS) a été choisie comme cible, en raison de sa grande taille et de sa faible altitude en orbite. La fréquence de fonctionnement de 20 MHz a été utilisée pour percer l'atmosphère et illuminer la cible sélectionnée. Des cartes Distance-Doppler ont été produites avec les mesures collectées, et des corrections ont été appliquées pour compenser les erreurs atmosphériques et de filtre. Les erreurs de distance ont été calculées à l'aide des estimations du contenu total des électrons (TEC) du logiciel libre australien Provision of High-Frequency Raytracing Laboratory for Propagation Studies (PHaRLAP). L'effet de l'ionosphère à différents niveaux d'activité solaire a été comparé par une période de transmission nocturne et une période de transmission diurne.

Il a été constaté que les transmissions nocturnes avaient surestimé les TEC et que des corrections n'étaient pas nécessaires, alors que les mesures des transmissions diurnes se sont avérées grandement affectées par les TEC plus grands. Les transmissions diurnes ont produit des retards de portée ionosphérique estimés allant jusqu'à 90 km et des corrections Doppler jusqu'à 45 Hz. Les transmissions nocturnes avaient des retards moyens de 30 km et des corrections Doppler d'un maximum de 15 Hz. Les mesures de distance finales après corrections avaient une racine de l'erreur quadratique moyenne (REQM) de 60,98 km sur une période de visibilité de 100 secondes pendant la transmission diurne et de 27,6 km sur une période de 450 secondes pendant la transmission nocturne. Avec des valeurs résiduelles aussi élevées, il a été constaté que HF ne convient pas pour des mesures de distance précises à moins que de meilleures méthodes de correction ionosphérique ne soient développées et que des techniques de traitement du signal plus intensives ne soient appliquées. Cependant, les mesures Doppler pour la transmission nocturne et diurne ont produit une REQM résiduelle inférieure à 10 Hz. Les résidus de taux de distance de transmission nocturnes avaient un REQM de seulement 85 m/s, ce qui est dans la marge d'erreur de la précision TLE. Cela suggère que HF peut être utilisé pour une détermination précise de l'orbite à l'aide de mesures Doppler.

Table of Contents

List of Figures

Chapter 2

Chapter 3

List of Tables

Chapter 2

Chapter 3

List of Acronyms

DND	Department of National Defence
SDA	Space Domain Awareness
TLE	Two-line elements
HF	High Frequency
NASA	National Aeronautics and Space Administration
OTHR	Over the Horizon Radar
LoS	Line of Sight
TEC	Total Electron Content
PHaRLAP	Provision of High-Frequency Raytracing Laboratory for Propagation Studies
DRDC	Defence Research and Development Canada
NEOSSat	Near Earth Object Surveillance Satellite
SSN	Space Surveillance Network
ISS	International Space Station
LEO	Low Earth Orbit
MUF	Maximum useable frequency
RSO	Resident Space Objects
SSM	Star-Stare Mode
TRM	Track-Rate Mode
SGP4	Simplified General Perturbations version 4
NESS	Near Earth Space Surveillance
HEOSS	High Earth Orbit Space Surveillance
WISE	Wide-Field Infrared Survey Explorer
SSOC	Sensor System Operations Centre
AF	Array Factor
FEKO	Feldberechnung für Körper mit beliebiger Oberfläche, German software for simulations
DSTO	Australian Defence Science and Technology Group
HPA	High Pass Amplifier
PRF	Pulse Repetition Frequency
EIRP	Equivalent isotropic radiated power
EKF	Extended Kalman Filter
FFT	Fast Fourier Transform
RMSE	Root Mean Square Error
IRI	International Reference Ionosphere

Chapter 1
Introduction

1.1 – Motivation

Many countries have declared space to be the fifth operational domain, after Land, Sea, Air and Cyberspace. With the evermore increasing popularity of space operations, for both military and civilian applications, control and awareness of activities in this domain has become essential for operational success. The most common civilian use of satellites includes applications such as weather monitoring and communications. This introduces an even higher requirement to maintain what has been termed Space Domain Awareness (SDA).

SDA refers to the complete knowledge of the positions and trajectory of spaceborne objects orbiting Earth. Defence Research and Development Canada (DRDC) has dedicated a group of researchers to maintaining accurate SDA as Canada moves towards more exploitation of the space domain. The increasing number of objects sent into space demands an increase in situation awareness of this operational domain to not only to keep Canada's operational assets safe, but also to keep an awareness of other surrounding operations.

1.2 – Identifying New Requirements

Canada currently has two active satellites used for SDA: NEOSSat and Sapphire [2]. Both these satellites use optical systems to gather data. Optical sensors capture reflected light to create images. This method allows optoelectronics systems to create images that are closer to how a human eye would view imagery, making it easier to decipher the collected data than other methods [3]. Other advantages to using optoelectronics for SDA include the simplicity of the system and potential for high resolution images. However, some disadvantages include their reliance on available light to produce accurate images and costly components [3]. When the sunlight is obstructed, the optical devices cannot obtain sufficient reflected light rays to form a clear image, potentially providing misleading information. The devices required to produce the high-resolution images come at a very high cost, making an optical imagery system potentially very expensive [3].

The use of ground and space-based radars in conjunction with the existing optical sensors for monitoring objects in geosynchronous orbit was explored by Livingstone in 2013 [4] to potentially counter the disadvantages of using only optical systems and increase Canada's ability to conduct SDA and in turn our contribution to the US Space Surveillance Network (SSN). Some of the proposed viable solutions have been further explored and implemented at DRDC [5].

As technology advances and interest in space operations increases, smaller and smaller spacecraft are being designed as a cost-effective means for space exploration, such as CubeSats [6]. With this comes an increase in requirements for more accurate SDA to perform accurate avoidance maneuvers for smaller objects (debris and spacecraft alike). The most accessible means of estimating a registered object's orbit is by using its Two Line Elements sets (TLE). TLEs are a set of orbital parameters that are propagated using special software to predict the orbit of the object at anytime in the future, this will be explained in more detail in section *2.1 – Predicted Orbital Parameters*. The level of accuracy of these estimates is approximately 1 km in position and 1 m/s in velocity, which will not be sufficient to maintain operational visibility and security on these smaller spacecraft [7]. These estimates refer to the range of the target and the velocity based on the orbital elements v_x, v_y, and v_z which are calculated using orbit determination methods. For this research, Doppler measurements were collected to estimate the radial velocity of the target, and no orbital determination was conducted. Two-way radial velocity errors of at least 10 m/s are typically measured for LEO satellites, and are what is expected to be measured in this research [7].

1.3 – Thesis Statement and Aim

This research tested the feasibility of using High Frequency (HF) Line of Sight (LoS) transmissions to detect and track spaceborne objects range to an accuracy higher than that provided by TLEs and radial velocity within the expected error margin of typical LEO satellites. It is hypothesized that HF is a viable frequency band to increase the accuracy of current SDA methods.

1.4 – Research Activities and Scope

The intent of this research is to increase the operational value of these already existing and expensive radar sites and provide an alternative means to achieve SDA. This would in-turn increase the operational security of Canada's space domain assets.

To achieve this, the existing Over the Horizon Radar (OTHR) at DRDC in Ottawa was used to actively search for a target in space. Using time delay measurements and Doppler frequencies, a range-Doppler map was produced with received power levels. The maximum power peaks indicated the initial measured location of the target. The target that was used for this experiment was the International Space Station (ISS) due to its large size and high probability of detectability. The following research areas were explored:

1. The existing radar system at DRDC Ottawa. The antenna and its operation will be discussed. Experiments were conducted with the existing system at DRDC. A preliminary evaluation of the radar capabilities was conducted to ensure the required resolution is achievable. Due to the configuration of the array, mutual coupling and the operation of the radar to avoid equipment failure was discussed;
2. Initial position calculations. Range-Doppler maps were produced to locate the initial estimated position and radial velocity of the target;
3. Radar range and Doppler frequency corrections. Due to the atmospheric complications with traversing the ionosphere at HF frequencies, range errors and other phenomena were explored and corrected to increase accuracy of target detection; and
4. Real time disturbances and orbit determination. It was expected to see noisy measurements at such low frequencies, and therefore the Kalman filter was explored as a potential real time curve smoothing correction technique, and as well as a possible position prediction filter for orbit determination.

1.5 – Organization

This document is organized into 4 major chapters. The first chapter, Chapter 1 – Introduction, the second chapter, Chapter 2 – Background Theory, the third chapter, Chapter 3 – Conducted Research, and Chapter 4 – Analyses and Concluding remarks. Chapter 2 will discuss background information to include supporting information on SDA and theoretical concepts that were employed throughout the research. Chapter 3 will discuss the conducted research in three phases: preliminary research, experiment development and execution, and results and verification. The final chapter will discuss the results and future research, and conclude this thesis.

Chapter 2
Background Theory

This chapter will discuss some background information pertinent to the conducted research. This will include discussions on orbit parameters, basic space transmissions, atmospheric considerations and corrections, an initial radar system evaluation, information on the selected target, the current solutions for SDA and previous work that has been conducted on HF for SDA.

2.1 – Predicted Orbital Parameters

Orbital parameters are generally encoded using a format called a Two-Line Element set (TLE). Using prediction algorithms, the state of an object's orbit at any point in the past or future can be estimated to some accuracy. TLE data is specific to the Simplified Perturbations models such as SGP, SGP4, SDP4, SGP8 and SDP8 [8].

Using SGP4 software, the initial orbit vectors of an object can be calculated. The prediction start and stop times are entered into the SGP4 software to ensure the orbit perturbations for that time are considered. The original mean motion n_o (angular speed required for a body to complete one orbit) and the semi-major axis a_o (distance from the center of the orbit ellipse to its furthest edge point) are first recovered from the input elements and then used to calculate the secular effects of atmospheric drag and gravitation. These equations can be found in [8], there are too many to be discussed here. This software considers factors affecting orbits such as eccentricity of the orbit, orbital inclination, orbit anomaly, argument of perigee, longitude of ascending node, atmospheric drag, equatorial radius of the Earth, and gravitational zonal harmonics of the Earth [8].

One of the TLEs for the ISS that was used for this research can be found in Figure 2.1. The first line of the TLE, referred to as Line 0, states the common name for the object based on the information from the Satellite Catalog, for this example the TLE for the ISS will be used.

```
ISS (ZARYA)
1 25544U 98067A   04236.56031392  .00020137  00000-0  16538-3 0  9993
2 25544  51.6335 344.7760 0007976 126.2523 325.9359 15.70406856328906
```

Figure 2.1 Example TLE for the ISS.

The next line, referred to as Line 1, includes the line number in column 0 (1), the satellite catalog number in columns 3-7 (25544), the ELSET classification in column 8 (U), the international designator in columns 10-17 (98067A), the Element Set Epoch in columns 19-32 (04236.56031392), 1st derivative of the mean motion with respect to time in columns 32-43 (.00020137), the 2nd derivative of the mean motion with respect to time in columns 45-52 (00000-0), the B drag term in columns 54-61 (16538-3), the element set type in column 63 (0), the element number in columns 65-68 (999) and the checksum in column 69 (3).

The third line, which is referred to as line 2, includes the line number in column 0 (2), the satellite catalog number in column 3-7 (25544), the orbit inclination in degrees in column 9-16 (51.6335), the right ascension of ascending node in degrees in columns 18-25 (344.7760), the eccentricity in columns 27-33 (.0007976), the argument of perigee in degrees in columns 35-42 (126.2523), the mean anomaly in degrees in columns 44-51 (325.9359), the mean motion in revolutions per day in columns 53-63 (15.70406856), the revolution numbers at Epoch in columns 64-68 (32890), and the checksum in column 69 (6).

Using the SGP4 software provided by the US Space Force through a website called Space-track [9], the ISS TLE was used to extract orbital data of the target's location and expected trajectory. For this

experiment, the TLEs were taken from N2Y0.com [10], which is a website dedicated to tracking satellites orbiting the Earth. Table 2.1 shows times, elevations and azimuths of multiple passes over the location of the transmitter and receiver at DRDC from Feb 2023 that were used for this experiment [10]. The full table includes 10-day predictions for all passes [10]. Similar data was obtained to determine the best day for data collection in November 2022. For each pass, the most recent TLE was used to reduce the time since epoch for highest accuracy.

Table 2.1 Snippet of the 10-day prediction for all passes of the ISS over DRDC OTHR location.

Start		**Max Altitude**			**End**	
Date UTC	Az	UTC	Az	EL	UTC	Az
9 Feb 14:38	WSW 250°	14:44	NW 329°	60°	14:49	ENE 61°
9 Feb 16:16	W 282°	16:21	N 357°	27°	16:26	ENE 68°
9 Feb 17:53	WNW 297°	17:58	NNE 17°	36°	18:04	E 93°
9 Feb 20:30	WNW 297°	20:35	SW 218°	57°	20:40	SE 132°

Using the most up to date TLE provided and the SGP4 software, the trajectory of the ISS can be estimated. As an example, the TLE from 9 Feb 2023 was used to calculate the expected azimuth and elevation positions of the ISS during a 10 min pass over the Ottawa receiver site:

```
Two Line Element Set (TLE):
1 25544U 98067A   23040.39562529  .00020695  00000-0  37246-3 0  9997
2 25544  51.6423 241.5065 0008219 331.4824  85.6013 15.49755163381978
```

Figure 2.2 TLE for ISS 09 Feb 2023.

By entering the start and stop times of a visible pass from Table 2.1, and the most up to date TLE for the ISS, the SGP4 software will calculate the azimuth, elevation, range, and range rate of the satellite for each time interval indicated.

Figure 2.3 is four plots showing the range, range rate, azimuth and elevation of the ISS as it passes on 9 Feb from 20:30 to 20:40 UTC, for a 10-minute observation period.

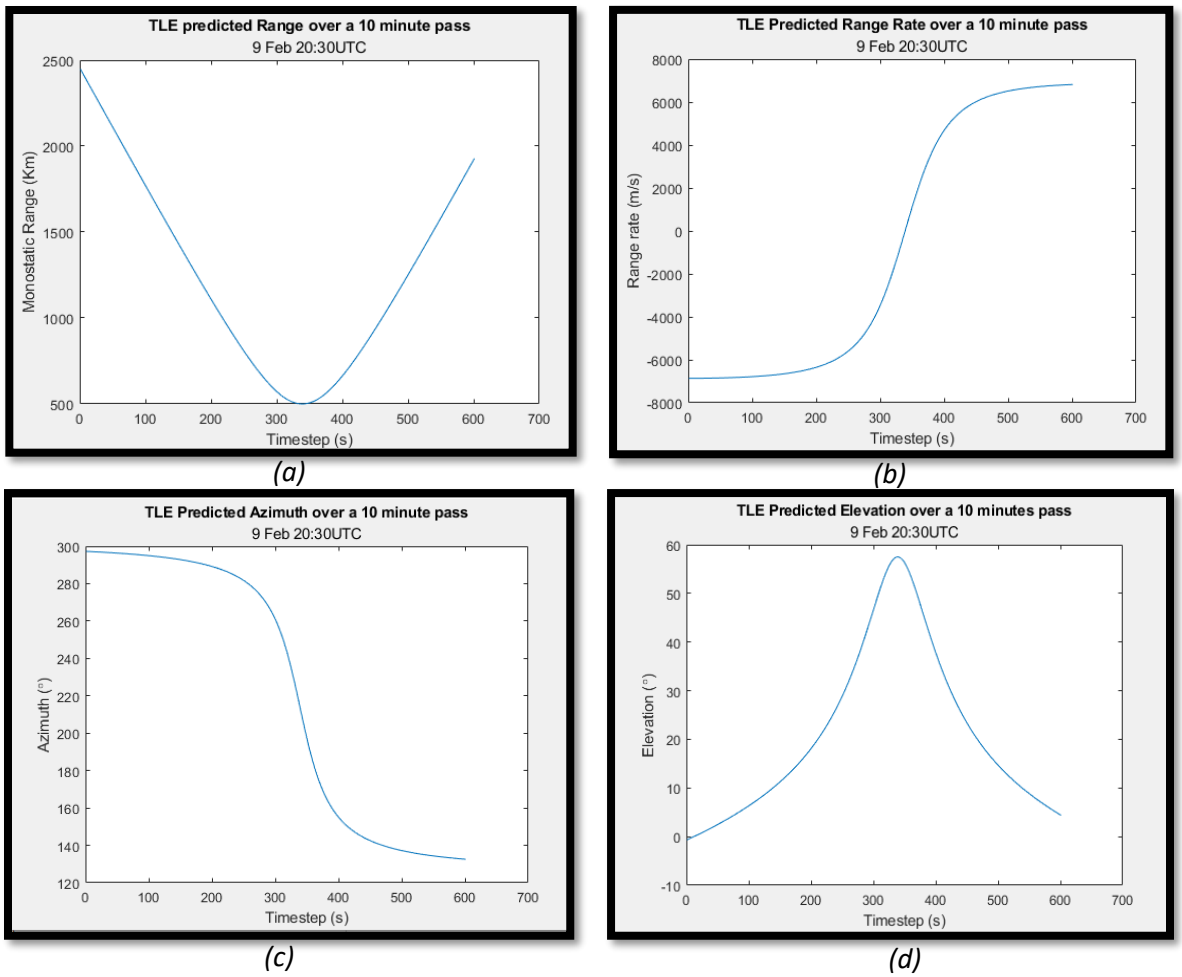

Figure 2.3 Orbital data calculated using Space-track SGP4 propagator for 9 Feb 2023 20:20UTC (a) TLE Predicted Range, (b) TLE Predicted Range Rate, (c) TLE Predicted Azimuth, (d) TLE Predicted Elevation.

This estimation was used as a guideline for what direction and trajectory to steer the radar beam to ensure the right orbiting body is being tracked. These estimations were also used to compare the HF measurements and final estimations for accuracy. The SGP4 software produces an accuracy up to 8 significant digits at epoch [8], and a range error up to 1 km. These predictions were used throughout this research as validation for the feasibility of using HF to locate and track space objects.

2.2 – Space Transmission

As detailed in [6] and [11], operating in the space environment presents a series of challenges to overcome. Communication distance is greatly increased, creating a requirement for high gain and high sensitivity in receivers [11]. Typical satellite communications are conducted over the UHF, S, X, Ku and Ka frequency bands, with satellite tracking, telemetry and command typically conducted over the S-band [11]. There has been a shift in recent years towards using S- and X-bands driven by a need for higher data rates [11]. However, at these higher frequencies there is greater atmospheric and rain attenuation adding to increased free space loss, factors that need to be compensated for by higher power transmission and higher gain antennas [11], [12].

This research utilized non-traditional frequencies for space transmissions and target detection by employing the HF band to pierce through the atmosphere, specifically the ionospheric layer, with LoS

propagation. Due to the lower transmission frequency, complications will be introduced as the signal will be more greatly affected by the ionosphere along its transmission path. The target selected for this experiment is a Low Earth Orbiting (LEO) target moving at speeds within the hypersonic range. This will need to be considered when processing the measured data.

2.3 – Atmospheric Considerations

The atmosphere is composed of five layers: the troposphere, the stratosphere, the mesosphere, the thermosphere, and the exosphere [13]. The tropospheric layer starts at the Earth's surface and extends from 8 to 14.5 km high and is the densest layer of the atmosphere and location of weather. This layer can cause an extra delay in the measurements of signals due to the presence of dry gases and water vapour in the form of clouds [14]. The stratosphere starts at the end of the troposphere and extends to 50 km high and is where the ozone layer is found. The mesosphere is the layer where the meteors burn up, and it extends to 85 km. The thermosphere starts just above the mesosphere and extends to 600 km. Found in both the mesosphere and the thermosphere, from 48 km to about 965 km, is the ionosphere, an ionized layer that causes range skewing and phase advances in RF signals.

The two layers that will impact the propagation of RF signals and will require corrections are the troposphere and the ionosphere. For this research, the frequencies that were used were 13 MHz and 20 MHz, and a main feature of the troposphere is that it is a non dispersive media with respect to electromagnetic (EM) waves up to 15 GHz, and therefore the effects of the troposphere for this research are not frequency dependent. The overall tropospheric delay will be modeled using software developed and provided by Dr. Malek Karaim from the RMC Navigation Research Team. However, since the delay will be minimal compared to the delay caused by the ionosphere, it will be corrected as part of the ionospheric corrections and not discussed any further.

The ionosphere is composed of different layers (D, E, F1, F2), each with different compositions. The sun radiation heats the gasses within these layers to the point that they lose electrons, and become ionized layers. With the presence of free electrons, the ionosphere has a dielectric constant and conductivity that is different than free space, changing how EM waves propagate through these layers. This medium can be considered a lossy medium defined by its own relative permittivity (ε') and conductivity (σ) [15]. These values are obtained based on the electron density of the ionosphere and the collision frequency in this ionized region and can be modelled by the following equations [15]:

$$\varepsilon' = 1 - \frac{N_e e^2}{\varepsilon_o m(\omega^2+v^2)} \tag{2.1}$$

$$\sigma = \frac{N_e e^2 v}{m(\omega^2+v^2)} \text{ ohm/m} \tag{2.2}$$

where N_e is the electron density (electrons/m^3), e is the fundamental electron charge (1.6x10^{-19} C), m is the mass of an electron (9x10^{-31} kg), ω is the angular frequency ($2\pi f$ rads/s), v is the collision frequency (s^{-1}), and ε_o is the permittivity of free space (8.854x10^{-12} F/m). As the electron density increases, the relative permittivity decreases, reducing the EM wave's ability to propagate within the medium. The conductivity shows the inverse relationship: as the electron density increases so does the conductivity, allowing for more free movement of the electrons.

The relative reduction in amplitude of an EM wave per meter as it travels through the ionosphere can be represented with an attenuation factor (α) and is modelled here as a function of conductivity and relative permittivity:

$$\alpha = \frac{60\pi\sigma}{\sqrt{\varepsilon'}}\ \mathrm{m}^{-1} \tag{2.3}$$

This factor is approximately inversely proportional to the square of the operating frequency, and therefore the higher frequencies experience less ionospheric attenuation. This thesis will be using a frequency of 20 MHz (within the HF frequency band), and therefore the transmitted signal will experience a much higher level of ionospheric attenuation than regular space transmission frequencies.

The ionosphere layers are depicted in Figure 2.4, which include the D, E and F1/F2 layers. Each layer effects transmissions specifically at frequencies below 30 MHz.

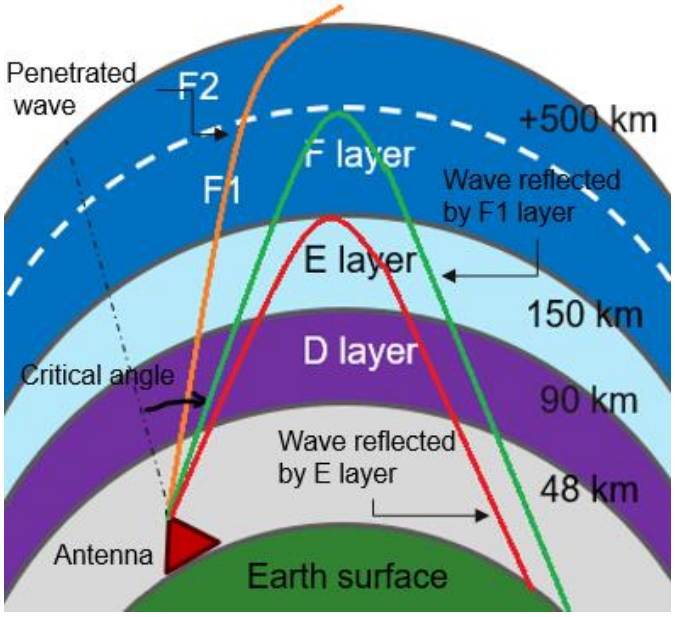

Figure 2.4 Composition of the Ionosphere (day) and skywave propagation.

The lowest layer is the D layer which is located 48 km to 90 km above the Earth's surface. This region does not achieve densities high enough to cause reflection or significant refraction, however it will attenuate the signal [16]. It is observed that higher frequencies see less absorption when penetrating the D layer. This layer sees electron densities below 10^4 cm^{-3} [15], with significant changes between the night and the day. The D layer disappears at night due the source of radiation being removed and the high rate of attachment.

The next layer is the E layer. This layer is found from 90 km to 150 km above the Earth's surface. This layer normally can only reflect signals below 10 MHz and can contribute to the attenuation and partial absorption of signals above that frequency [16]. The E layer sees electron densities in the 10^5 cm^{-3} range [15], and becomes weakened during the night, due to the primary source of ionization not being present. After sunset an increase in the height of E layer maximum increases the range in which radio waves can travel by refraction from this layer.

The last layer is the F layer. This layer consists of two sublayers, F1 and F2. At night only F2 remains while F1 disappears. It extends from 150 km to more than 500 km above the Earth's surface [16]. This layer has the highest electron density of 10^6 cm^{-3} and above [15], and any signal penetrating this layer will be lost to space.

The height distribution of electron densities within each layer is shown at *Figure 4.6 Height Distribution of Electron Densities* of [15]. This graph demonstrates the increase in free electrons from the first layer D to the top of the F2 layer. The electron density then decreases as it reaches the boundary of the ionosphere, where solar radiation is less apparent.

When conducting routine OTHR communications, the intent is to refract the EM waves off the ionosphere using what is called a skywave. Skywaves are created when HF radio waves are refracted back down towards the Earth instead of piercing through the ionosphere, covering a large communication range that spans beyond the horizon, Figure2.4 depicts an example of skywaves refracting off the E and F1 layer. Often the maximum usable frequency needs to be calculated to ensure that the propagation will not pierce through the ionosphere:

$$MUF = \frac{f_c}{\sin\theta} \tag{2.4}$$

Where MUF is the maximum usable frequency for skywave propagation, f_c is the critical frequency, and θ is the target elevation angle. The critical frequency is the frequency of transmission where the RF waves will begin to pierce the ionosphere and is often measured by sending a continuous chirp of varying frequencies in the HF frequency band vertically into the sky and recording the straight-down return signal [12]. The intent for this research is to conduct LoS transmission through the ionosphere, and therefore it was required be above the MUF. The MUF will change based on time of day as well as solar activity and atmospheric conditions. The critical angle is the value of θ that represents the highest elevation for skywave propagation at the specified frequencies, see Figure 2.4. In order to ensure the transmission pierces the ionosphere, the target will need to be visible above the critical angle.

Using (2.4), a transmitting frequency of 20 MHz (the frequency used for this experiment), and an estimated critical frequency of 10 MHz (daytime, estimate from [17]), the target should not be detectable below elevation of 30°, (example only). This will provide restrictions on the elevations that the radar system will be able to locate and track the ISS and was considered when operating the radar.

2.4 – Ionospheric Corrections

Refraction and Range correction

Once the range of the target is measured, atmospheric effects will need to be considered and corrected, specifically due to the nature of the HF waves interacting with the ionosphere. Due to the time varying and dispersive properties of the ionosphere, accurately modeling the amount of attenuation, delay and angular distortion is a vital part in many studies of radio waves propagating in the ionosphere.

The theory behind ionospheric refraction was first developed by Lassen, Hartree, and Appleton independently in the 1920s and 1930s coining the formulas now known as the Appleton-Hartree or Appleton-Lassen formulae. These formulae are mathematical expressions that describe the refractive index for electromagnetic propagation in a cold magnetized plasma.

[18] discusses a method to correct the ionospheric time delay and offset errors caused by refraction based on radar dual-frequency detection. Radar target range measurements at two adjacent frequencies are utilized for calculating the electron density integral exactly along the propagation path of the radar wave, which can generate accurate ionospheric range corrections. In this study, a space target surveillance radar of P band was utilized to validate the proposed method. The results of their testing showed that this method was able to estimate residual ranging error with a RMSE of between 3.11 m and 6.43 m [18]. Figure 2.5 is a graphical representation of how the ionosphere can distort the radio waves path and cause errors in range and angle estimations.

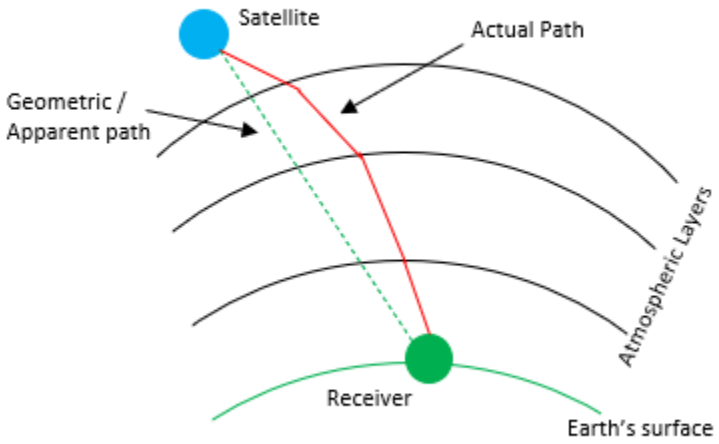

Figure 2.5 Graphical representation of range error due to atmospheric effects, one way.

For trans-ionospheric propagation for frequencies below 3 GHz, ionospheric effects that cause errors in range calculations include: time delay, phase advance, Faraday rotation, and scintillation. The time delay error is the main ionospheric error source for the ranging of space objects and to the first order approximation is directly proportional to the total electron content (TEC) along the radar wave path [18]. Traditionally, the two methods that are used to estimate TEC are: ionosonde-based TEC estimation, and GNSS-derived TEC. However, these methods both have high level of uncertainty and are not capable of satisfying the requirements of correction accuracy for the advanced space target radar systems, and hence further attempts at a more accurate method has been explored [18].

The Appleton-Hartree equation for the index of refraction is modelled by the following equation [19]:

$$n = \sqrt{1 - \frac{X}{1 - jZ - \frac{\frac{1}{2}Y^2 sin^2\theta}{1-X-jZ} \pm \frac{1}{1-X-jZ}\sqrt{\frac{1}{4}Y^4 sin^4\theta + Y^2 cos^2\theta (1-X-jZ)^2}}} \tag{2.5}$$

The variables in (2.5) are found in Table 2.2

Table 2.2 Variable definitions for (2.5).

Symbol	Variable value/name	Units
$\boldsymbol{n}$	Complex refractive index	No units
$\boldsymbol{j = \sqrt{-1}}$	Imaginary unit, extinction coefficient of the material	No units
$\boldsymbol{X}$	$\frac{\omega_o^2}{\omega^2}$	No units
$\boldsymbol{Y}$	$\frac{\omega_H}{\omega}$	No units
$\boldsymbol{Z}$	$\frac{v}{\omega}$	rad/s^2
$\boldsymbol{v}$	electron collision frequency	s^{-1}
$\boldsymbol{\omega}$	$2\pi f$, angular frequency	rad/s
$\boldsymbol{f}$	ordinary frequency	Hz
$\boldsymbol{\omega_o}$	$\sqrt{\frac{Ne^2}{\varepsilon_o m}}$, electron plasma frequency	rad/s
$\boldsymbol{\omega_H}$	$\frac{\lvert e \rvert B_o}{m}$, electron gyro frequency	rad/s
$\boldsymbol{\varepsilon_o}$	permittivity of free space (8.854x10^{-12})	F/m
$\boldsymbol{B_o}$	Ambient magnetic field strength	A/m
$\boldsymbol{e}$	electron charge (1.6x10^{19})	C
$\boldsymbol{N}$	electron density	cm^{-3}
$\boldsymbol{m}$	electron mass (9x10^{-31})	kg
$\boldsymbol{\theta}$	Angle between the ambient magnetic field vector and the wave vector	rads

The group velocity V_G of a wave is the velocity with which the overall envelope shape of the wave's amplitudes, known as the modulation or envelope of the wave, propagates through space. It is defined in terms as the first derivative of the angular frequency ω in terms of the wave number k as:

$$V_G = \frac{\partial_\omega}{\partial_k} \tag{2.6}$$

According to Davis [18], the group velocity V_G of ionospheric radio waves of and ionospheric refraction index n have the following relationship:

$$V_G \approx cn = c\sqrt{1 - \frac{Ne^2}{\varepsilon_o m\omega^2}} \tag{2.7}$$

With binomial expansion:

$$V_G = c\sqrt{1 - \frac{Ne^2}{\varepsilon_o m\omega^2}} = c(1 - \frac{Ne^2}{2\varepsilon_o m\omega^2} - \frac{1}{8}\left(\frac{Ne^2}{\varepsilon_o m\omega^2}\right)^2 - \frac{3}{8}\left(\frac{Ne^2}{\varepsilon_o m\omega^2}\right)^3 + \cdots) \tag{2.8}$$

At UHF and VHF frequencies $\omega^2 \gg \frac{Ne^2}{\varepsilon_o m}$ therefore the first order approximation can be used:

$$V_G \approx c(1 - \frac{Ne^2}{2\varepsilon_o m\omega^2}) = c(1 - 40.3\frac{N}{f^2}) \tag{2.9}$$

where N is the electron density and f is the radio wave frequency.

The distance R_o to the target can be modelled in terms of propagation time of radio wave transmitted from radar to the target, Δt.

$$R_o = \int_0^{\Delta t} V_G \partial t = c \int_0^{\Delta t} \left(1 - 40.3 \frac{N}{f^2}\right) \partial t = c \cdot \Delta t - \frac{40.3}{f^2} N_T \tag{2.9}$$

where $N_T = \int_0^{\Delta t} N \partial t$ is the Total Electron Content (TEC) along the propagation path, $\frac{40.3}{f^2} N_T$ is the ionospheric delay to the first order and $c \cdot \Delta t$ is the radar measurement of target distance. By setting $R_e = c \cdot \Delta t$ and re-arranging (2.9) an expression for the radar measurement of target distance in terms of the actual target distance R_o and the ionospheric delay can be modeled:

$$R_e = R_o + \frac{40.3}{f^2} N_T \tag{2.10}$$

When the radar transmits the radio waves of two different frequencies f_1 and f_2 simultaneously, where $f_2 = a_s f_1$, the radar measurements of target distance is then modelled as below based on (2.10):

$$\begin{cases} R_{e1} = R_o + \frac{40.3}{f_1^2} N_T \\ R_{e2} = R_o + \frac{40.3}{f_2^2} N_T = R_o + \frac{40.3}{(a_s f_1)^2} N_T \end{cases} \tag{2.11}$$

Transmitting at two different frequencies provides ionospheric distance errors modelled by the second part of each equation in (2.11) $\Delta R_{f_1} = \frac{40.3}{f_1^2} N_T$ and $\Delta R_{f_2} = \frac{40.3}{f_2^2} N_T$. Since the propagation of both transmissions will be nearly identical, an assumption that N_T will be the same is made. A relationship ratio can therefore be modelled:

$$\frac{\Delta R_{f1}}{\Delta R_{f2}} = \frac{\frac{40.3}{f_1^2} N_T}{\frac{40.3}{f_2^2} N_T} = \frac{f_2^2}{f_1^2} \tag{2.12}$$

Using substitution and the formulas $\Delta r = \Delta R_{f1} - \Delta R_{f2}$ and $\Delta f = f_2 - f_1$, the number of variables can be reduced into the following expression:

$$\frac{\Delta R_{f1}}{\Delta R_{f1} - \Delta r} = \frac{(f_1 + \Delta f)^2}{f_1^2} \tag{2.13}$$

Which can be rearranged to determine the relationship between the ionospheric distance errors at two-frequency (Δr) with the difference of the two frequencies (Δf):

$$\Delta r = \Delta R_{f1} \cdot \left(1 - \frac{f_1^2}{(f_1 + \Delta f)^2}\right) \tag{2.14}$$

Figure 2.6 the graph in [18] representing the relationship between Δf and Δr has been reproduced using 20 MHz instead of 500 MHz. This shows very similar results to that of 500 MHz, where with the increasing of ionospheric distance error ΔR_{f1}, the difference between the dual frequencies can be lower.

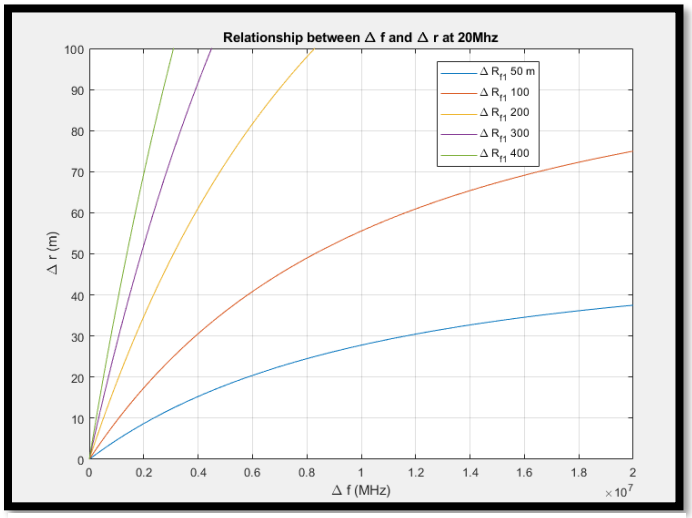

Figure 2.6 Relationship between Δf and Δr at 20 MHz.

Therefore, it is possible to use this two-frequency method to also estimate the TEC (N_T) by rearranging equation (2.9):

$$R_o = c \cdot \Delta t - \frac{40.3}{f^2} N_T$$

To produce an expression for TEC with two frequencies:

$$N_T = \frac{c(\Delta t_2 - \Delta t_1)}{40.3\left(\frac{1}{f_2^2} - \frac{1}{f_1^2}\right)} \tag{2.15}$$

However, Δf must be large enough to produce a difference between Δt_1 and Δt_2. For example, if the two frequencies selected were 20 MHz and 19 MHz, only a time delay of 0.363 μs would be observed when using a low value of $N_T = 10^{16}$. This would be very difficult to measure with the current system in Ottawa, due to the limited bandwidth of 10 kHz.

An alternative method is to use the phase shift between received signals instead of time delay. The phase angle between two waves can be calculated using the following formula:

$$\Delta\Phi = 2\pi \cdot f \cdot \Delta t \tag{2.16}$$

where the phase differences between the two signals can be modelled:

$$\Delta\Phi_2 - \Delta\Phi_1 = -2\pi(f_2\Delta t_2 - f_1\Delta t_1) \tag{2.17}$$

Using the same values of $f_1 = 20\ MHz$ and $f_2 = 19\ MHz$ in (2.14) and substituting $\Delta t_1 = \frac{1}{c}(R_o + \frac{40.3N_T}{f_1^2})$ and $\Delta t_2 = \frac{1}{c}(R_o + \frac{40.3N_T}{f_2^2})$ the phase difference between the two signals can be estimated using equation (2.17):

$$\Delta\Phi_2 - \Delta\Phi_1 = \frac{-2\pi}{c}(f_2\left(R_o + \frac{40.3N_T}{f_2^2}\right) - f_1\left(R_o + \frac{40.3N_T}{f_1^2}\right))$$

If $R_o = 1000$km, and $N_T = 10^{16}$ the phase difference can be calculated to be $\Delta\Phi_2 - \Delta\Phi_1 = 1{,}198{,}727.37°$, which is highly ambiguous. Since HF frequencies have rather large

wavelengths, using a smaller difference in frequencies may provide a less ambiguous result in the phase difference. If $f_1 - f_2 = 50$ Hz, the phase difference is calculated to be $\Delta\Phi_2 - \Delta\Phi_1 = 59.9°$, which is now unambiguous.

However, for this method of estimation to work, there needs to be some prior knowledge of the target range to estimate the TEC. It would therefore be possible to estimate the TEC using a target of known range prior to conducting experiments with targets of unknown range to estimate possible range correction requirements.

The first order approximation is sufficient to calculate an accurate estimation when using UHF and VHF. However, it is unconfirmed that this is the same case when using HF frequencies. To confirm the dual frequency method is valid for HF transmissions, a confirmation of the calculated TEC needs to be conducted. To validate this first order approximation, the TEC is estimated using the dual frequency approach discussed here with two set of frequency shifts, using three different frequencies. It would be expected that if the TEC calculated using f_1 and f_2 is equal to the TEC calculated using f_2 and f_3 then the first order approximation is valid. This will also be validated using an Australian Government open-source ray-tracing program called PHaRLAP to estimate the TEC for the transmission.

Since it is not possible to transmit two frequencies simultaneously using the existing infrastructure at DRDC, due to very large temporal forward and reverse power level variations, the design of the waveform had to be considered so that it alternated between the three selected frequencies. This concept can be implemented as either an intra-pulse frequency shifting or inter-pulse frequency shifting. Intra-pulse frequency shifting uses one pulse repetition time (PRT) slot to transmit the two frequencies side by side [18]. To do this, the bandwidth of the radar needs to be larger than the difference between the frequencies (Δf) or the receiver needs to be capable of processing the signals of the different channels of narrow bandwidth. Inter-pulse frequency shifting uses two neighboring PRT slots to transmit the two frequencies. This is achievable with systems that have good frequency agility, but has a higher consumption of time, leading to larger distances between the two frequencies and slightly less accurate estimations [18]. These schemes are presented in Figure 2.7 (a)intra-pulse frequency shifting, (b)inter-pulse frequency shifting, re-created from [18].

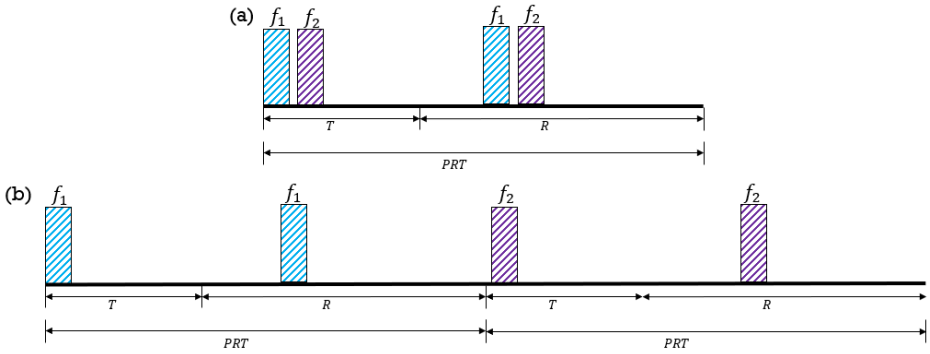

Figure 2.7 Representation of (a) intra-pulse frequency shifting and (b) inter-pulse frequency shifting. PRT= pulse repetition time, T = transmit, R=receive. Diagram recreated from [17].

The system at DRDC uses two different antennas for transmitting and receiving, meaning there is no requirement for the transmitter to stop and listen for a response. The waveform that was used for this part of the experiment was a Linear Frequency Modulated Continuous Waveform (LFMCW), shifting

between three different waveforms every 0.02 s to change the transmission frequency. Therefore, it was not be possible to conduct intra-pulse waveforms. Instead, to do the inter-pulse method the following waveform frequency shift scheme was designed by Dr. Simon Henault at DRDC is modeled in Figure 2.8.

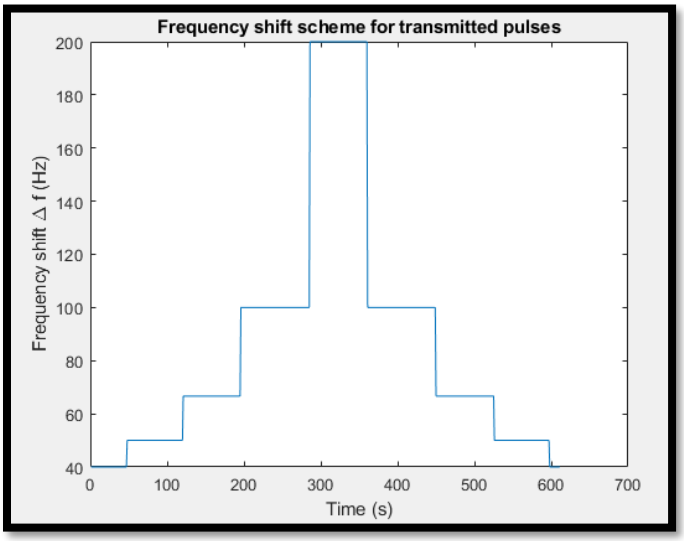

Figure 2.8 frequency shift scheme for experiment, provided by Dr. Henault.

The waveform was modulated to begin with a difference in frequencies of 40 Hz when the target was the furthest and the TEC was expected to be the highest and increased to a difference of 200 Hz when it was the closest and when the TEC was expected to be the lowest. This waveform is expected to increase the accuracy of the TEC measurements, as exampled in Figure 2.6.

Distance Offset and Matched Filter Errors

The time delay of the frequency shifting needs to be considered for both intra-pulse and inter-pulse frequency shifting to calculate the distance offset compensation, Δr_1, that needs to be applied before being able to apply the ionospheric range correction techniques. The target moving distance can be modeled with the following equation [18] :

$$\Delta r_1 = \tilde{V}_r \cdot t \tag{2.18}$$

where $\tilde{V}_r$ is the radial velocity of radar target that is calculated using the measured Doppler frequencies. For intra-pulse frequency shifting t is the sum of pulse width and pulse interval and for inter-pulse frequency shifting t is equal to the actual PRT.

A second ranging error, Δr_2, that is present due to a moving target and the system parameters is known as range-Doppler coupling or a matched filter error. Using a linear frequency modulation (LFM) will introduce this ranging error in the matched filter due to the Doppler frequency shifting by the target movement. These errors will account for a large portion of the required corrections due to the high velocities being measured. This range offset can be presented as follows [20]:

$$\Delta r_2 = \frac{T_p \cdot \tilde{V}_r \cdot f}{B} \tag{2.19}$$

where T_p is the pulse width and B is the bandwidth. Once the distance offset is compensated, the process to correct ionospheric ranging errors can be implemented.

Phase Advance

In a vacuum, radio signals propagate at the speed of light, however in the presence of plasma in the ionosphere, the signals are affected by group delay and phase advance due to attenuation, absorption and scintillation (the rapid varying of amplitude and phase of a received signal). The level of these effects is signal frequency dependent and to a first order approximation is proportional to the TEC (N_T) along the propagation path. The amount of this phase advance is also called a phase path decrease, and is modelled here [21]:

$$\phi = \frac{1.34\times10^{-7}}{f} N_T \ (Cycles) \tag{2.20}$$

where N_T is measured in el/m^2 column.

Since frequency is a time derivative of phase, it directly effects the measured Doppler frequency and will need to be corrected. This effect will see larger corrections required during the daytime hours due to the stronger ionization in the atmosphere, and the presence of all the ionospheric layers. However, at night the effect will be minimized to only a few Hz error. This effect is stronger with lower frequencies within the HF band, and becomes almost negligible in higher frequency bands. The change in frequency due to the phase advance can be modelled here:

$$\Delta f = \frac{d\phi}{dt} = \frac{1.34\times10^{-7}}{f} \frac{d}{dt} N_T \ (Hertz) \tag{2.21}$$

This correction was applied to the Doppler measurements to account for this phenomenon.

2.5 – International Space Station

The ISS is a satellite that orbits Earth within the LEO region (orbits below 2000 km), at an altitude of approximately 408 km moving at a velocity of 7.78 km/s, meaning the ISS orbits Earth every 90 minutes [22]. Objects within the LEO region are closely tracked as they pose a collision risk to many of the existing satellites. The ISS is the largest module space station currently in LEO, making it an ideal target for experimental tracking. It has a measured Radar Cross Section (RCS) of approximately 402 m^2 [10], which would make it easy to locate and identify as the correct target. Due to the high velocity of the target, the CPI was limited to 1 s to ensure no Doppler-range migration.

2.6 – Orbit Determination

There are two main approaches to solve orbit determination: the geometric or kinematic approach and the dynamic approach [23]. The kinematic approach, shown in Figure 2.9 (a), is purely geometric and uses no dynamical description of the spacecraft's motion. The approach relies purely on observation data to estimate the state vectors at each epoch. This approach therefore requires high data sampling as well as the availability of accurate measurements. The second approach, shown in Figure 2.9 (b) is the dynamic approach, which uses a dynamic model to describe the motion of the spacecraft, since there is usually only one measurement available per epoch. For this research, the dynamic approach is used due to data available and the limitation of only one ground station available.

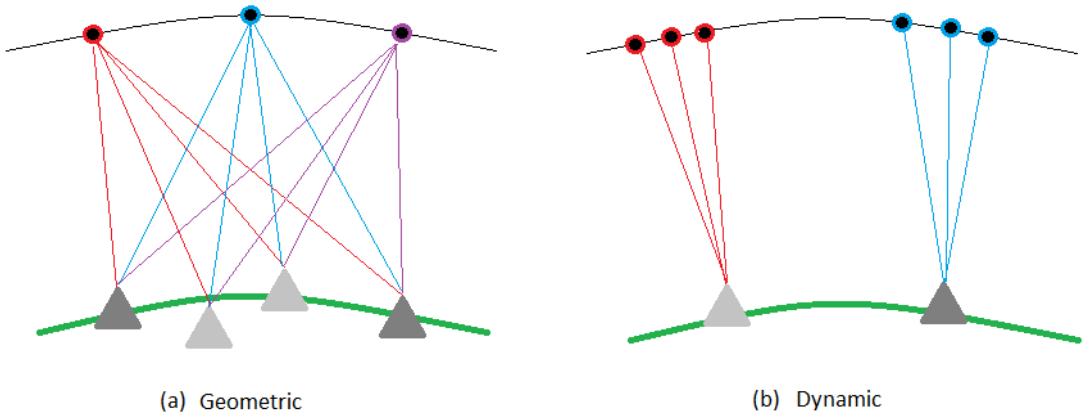

Figure 2.9 Main approaches to orbit determination (a) Geometric and (b) Dynamic.

Kalman Filter for Range Smoothing and Position Determination

The Kalman Filter is a set of recursive equations that provides estimates of unknown variables given measurements observed over time. These filters can be used for filtering out noise, predicting new positions, and smoothing curves [24]. When using the Kalman filer as a tracking mechanism, there are two typical models that are employed: position and constant speed estimates; and position, speed and constant acceleration estimates. This motion can be represented by a general state space model [24]:

$$\vec{x}_{k+1} = \phi_k \vec{x}_k + B_k \vec{u}_k + D_k \vec{w}_k \tag{2.22}$$

where $\vec{x}_{k+1}$, $\vec{x}_k$ are the state at sample k and $k+1$(prediction), $\phi_k$is the state transition matrix, created based on the required states, $B_k$is the input matrix, $\vec{u}_k$ is the known inputs, such as accelerations, $D_k$is the system disturbance matrix and $\vec{w}_k$is the system noise [24].

It is typically not possible to measure the state variables directly, therefore the measurements are given by the following equation [24]:

$$\vec{z}_k = H_k \vec{x}_k + \vec{v}_k \tag{2.23}$$

where $\vec{z}_k$are the measurements, $H_k$is the measurement matrix and $\vec{v}_k$is the measurement noise.

Using a variation of the state space equation (2.22), we can use Kalman Filters to calculate an estimate of the state space variables at time $k+1$ using the estimate from time k and measurements from the radar system to find the state prediction x_k [24]:

$$\vec{x}_{k+1|k} = \phi_k \vec{x}_{k|k-1} + B_k \vec{u}_k + K_k(z_k - H_k \hat{x}_k) \tag{2.24}$$

The third term of (2.24) includes the Kalman Gain (K_k) and a residual error factor ($z_k - H_k \hat{x}_k$). The Kalman gain is calculated for each iteration to minimize the mean square error (MSE) of each state parameter. The orthogonality principle is applied when deriving the Kalman gain to ensure reduced error. To apply this principle, we introduce an error covariance matrix, P_k, which is the expected value of the estimate of the state vector at time k, and can be represented by the following equation [24]:

$$P_k = E\left\{(\hat{\vec{x}}_k - \vec{x}_k)(\hat{\vec{x}}_k - \vec{x}_k)^T\right\} \tag{2.25}$$

The P_k values are also predicted iteratively throughout the process. As the number of samples increase, we expect to see P_k converge towards a set of values that will reduce the MSE until it becomes irreducible [24]. In addition to the error covariance matrix, we must also introduce a noise and system covariance matrices to account for system and measurement noises. Equation (2.22) through (2.25) can be represented by the set of iterative equations found in Figure 2.10, re-created from [24]. For this research, the Kalman filter was implemented as both a method to smooth the noisy range measurements, as well as to estimate position using only the measured Doppler and Range data.

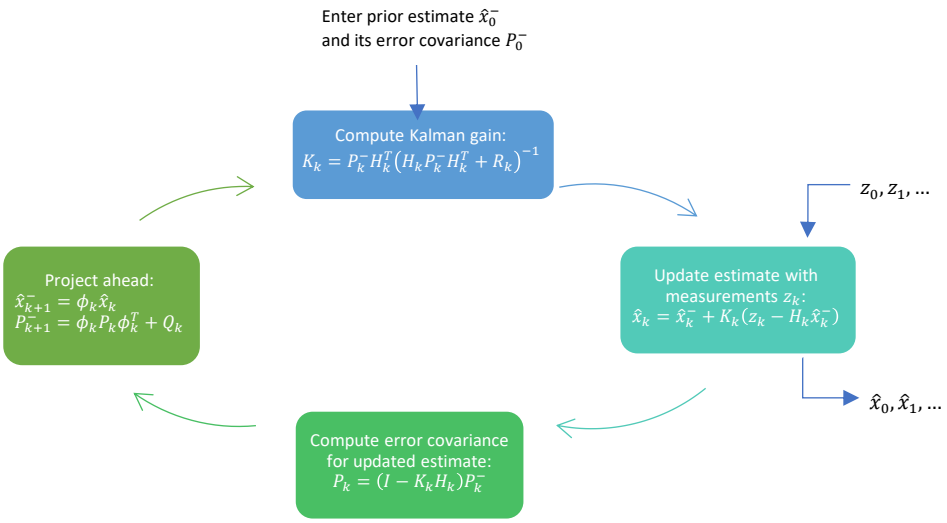

Figure 2.10 Kalman Loop.

2.7 – Radar System Evaluation

Radar Range Equation

The radar range equation serves the purpose of estimating the range of a radar as a function of the radar characteristics and is very useful as a guide for designing a radar system. The basic form is given here [16]:

$$R_{max} = \left[\frac{P_t G \sigma A_e}{(4\pi)^2 S_{min}}\right]^{1/4} \tag{2.26}$$

where R_{max} is the maximum detectable range (m), P_t is the peak transmitted power (W), G is the antenna gain (unitless), σ is the RCS (m^2), A_e is the effective aperture area (m^2), and S_{min} is the minimum detectable signal (W).

This equation represents a radar that uses the same antenna for both transmitting and receiving, called a monostatic radar. The relationship between the gain of the antenna and its effective area can be modelled using the following equation:

$$G = \frac{4\pi A_e}{\lambda^2} \tag{2.27}$$

where λ is the wavelength of the radar signal (m). By substituting (2.27) into (2.26), the range equation can be modified to be expressed in terms of effective aperture only:

$$R_{max} = \left[\frac{P_t \sigma A_e}{(4\pi)^2 S_{min}} \left(\frac{4\pi A_e}{\lambda^2}\right)\right]^{1/4} = \left[\frac{P_t \sigma A_e^2}{4\pi\lambda^2 S_{min}}\right]^{1/4} \quad (2.28)$$

By re-arranging (2.28), and substituting into (2.26), a similar alternate form of the radar range equation can be produced in terms of gain only:

$$A_e = \frac{G\lambda^2}{4\pi} \quad (2.29)$$

$$R_{max} = \left[\frac{P_t G \sigma}{(4\pi)^2 S_{min}} \left(\frac{G\lambda^2}{4\pi}\right)\right]^{1/4} = R_{max} = \left[\frac{P_t G^2 \lambda^2 \sigma}{(4\pi)^3 S_{min}}\right]^{1/4} \quad (2.30)$$

The basic form of the radar equation will be modified for each application of radar to suit the many different applications radars are employed for.

The radar that was used for this research had two different antennas at two different locations for the transmitter and the receiver. This is called a bi-static radar. However, since the distance between the two antennas is much smaller than the range of the expected target, the radar configuration is considered a pseudo monostatic-static radar system, meaning it acts as a monostatic system with non-identical antennas. The radar equation therefore needs to only change slightly to reflect the non-identical antennas: instead of using identical gain values (G^2), a gain value for both the transmitter and receiver needs to be considered ($G_t G_r$).

An alternate form of the radar range equation can be used to point to aspects of HF radar that are significantly different from radars that use higher frequencies. These differences include adaptation to the environment, frequency and waveform selection, radar cross section, path losses, multipath effects, noise, interference, antenna gains, spatial resolution, and clutter [16]. The following equation is a modified range equation for HF specific propagation:

$$\frac{S}{N} = \frac{P_{av} G_t G_r T \lambda^2 \sigma F_p}{(4\pi)^3 L_p L_s N_o R^4} \quad (2.31)$$

Where $\frac{S}{N}$ is the signal to noise ratio (unitless), $P_{av}$is the average power transmitted (W), T is the coherent processing time (s) (the total time to be sampled), G_t is the transmitter gain (unitless), G_r is the receiver gain (unitless) (since Rx and Tx antennas are not identical), $F_p$is the propagation factor (rads/m), $N_o$is the noise power per unit bandwidth, and $L_p L_s$ are the transmission path and system losses (unitless).

As per online sources [10], the RCS of the ISS is approximately $402\ \mathrm{m}^2$. This was used to ensure the correct target had located and tracked. Transmission will be operating at 20 MHz, with non-identical receive and transmit antennas. The gain values will be dependent on the operation frequency and the elevation but can be estimated at 17 dB and 20 dB for calculations based on simulated data.

Using (2.31) with the following theoretical values it is estimated that the maximum range the system can achieve is 3264.2 km:

$P_{av} = 64$ kW
$G_t(\theta, \varphi)G_r(\theta, \varphi)$ calculated from Figure 3.5 below
$T = 1$ s
$\lambda = 15$ m
$\sigma = 401.2$ m^2
$F_p =$ assume 1 for theoretical calculations
$L_p L_s = 3$ dB
$\frac{S}{N} = 14$ dB, minimum required for good detection
$N_o = -148 - 12.6 \ln\left({}^{f(\mathrm{MHz})}/_{3}\right)$
$f = 20$ MHz

Noise contribution (N_o) is a combination of thermal and environment noise, however in HF propagation the environment noise dominates. Instead of using the noise figure that does not affect the environmental noise, for this estimate the empirical environment noise levels will be used, such as residential, rural, remote, etc. For this thesis, the environmental noise model selected was for rural communities [16].

Using the ray tracing software PHaRLAP developed by DSTO [25], the propagation factor is estimated to be almost 0 dB at 20 MHz, and therefore is negligible to the final range. The altitude of the ISS from the official NASA database [22] indicates an orbiting altitude of 408 km, which is within the maximum achievable range. However, the ISS may only be directly above the receiver for a portion of the pass, or not at all. Therefore, the maximum slant range needs to be determined. The slant ranges were calculated at each elevation and they were found to be between 408 km and 3000 km when the elevation was between 10° and 90°.

A PRF of 50 pulses per second (denoted as f_{prf}) was used, the unambiguous range was calculated to be 3000 km using the following equation:

$$R_u = \frac{c}{2f_{prf}} = \frac{3.0\times10^8}{2(50)} = 3000 \text{ km} \tag{2.32}$$

As per the calculations presented above, the ISS is within unambiguous and maximum detectable range throughout the pass over Ottawa between 10° and 90°. The ISS should visible for majority of the pass.

The radar used for this research is linearly polarized, and therefore due to Faraday rotation within the atmosphere, power fluctuations may occur when the received signal is rotated.

Radar Resolution and Accuracy

Prior to beginning the experiment, a preliminary evaluation of the radar functionality was conducted to ensure adequate resolution and accuracy could be achieved. Range resolution is the radars' ability to distinguish between two targets that are very close in position and accuracy refers to the degree in which the measured data conforms with the actual data [26]. This will be important when tracking smaller debris that may be enclosing in on the satellite that is being tracked or when tracking smaller targets. Since the radar system in use for this thesis is pseudo mono-static, the accuracy and resolution will be calculated using the monostatic equations. The range resolution is calculated with the following equation:

$$\Delta R = \frac{c}{2B} \tag{2.33}$$

where ΔR is the range resolution, c is the speed of light and B is the bandwidth of 10 KHz. This provides a resolution of 15 km. For this research, only one target is being tracked, therefore the range resolution was not as important as the accuracy of the measurements. Range accuracy is inversely related to the bandwidth of the transmitted signal and the square root of the signal to noise ratio, represented in the following equation [27]:

$$\delta R \cong \frac{c}{2B\sqrt{2SNR}} \tag{2.34}$$

where δR is the measuring error, c is the speed of light, B is the bandwidth and SNR is the signal to noise ratio.

Based on discussion later on in section *3.1.1 – HF radar operation* in this thesis, the SNR is expected to be as high as 40 dB at certain points in the pass. Substituting this value for SNR (convert to linear with $10^{SNR/10}$ first) and a bandwidth of 10 KHz into (2.34), it is expected that this radar can measure the ISS with an accuracy of 105 m. For smaller objects, a larger system may be required to achieve the desired accuracy.

DRDC has plans to re-create this array using 4 times more elements and power available for transmission in the Arctic. The increase in power as well as the more isolated location of the radar would provide the radar with an additional 30 dB in gain. With this gain increase, there would be a SNR increase, which in turn would increase the accuracy of the radar measurements.

Due to the large wavelength of 15 m, it is expected that the RCS of targets less than 10 m will quickly drop. However, previous work done conducted by the Australian Defence Science and Technology Group (DSTO) showed that targets as small as 2 m could be detected using 30 MHz with a system having a similar size, this is discussed later on in section *2.8 – Previous work with SDA* [28].This suggests that with the larger system planned for construction, a higher-level accuracy is possible.

The other component that is being measured during this experiment is the radial velocity of the target. This is estimated using the measured Doppler frequencies. The radial velocity resolution is modelled here [27]:

$$\Delta V = \frac{\lambda}{2CPI} \tag{2.35}$$

where ΔV is the velocity resolution, λ is the wavelength of 15 m, and CPI refers to the dwell time on target (1s). This would therefore provide a radial velocity resolution of approximately 7.5 m/s.

The accuracy of radial velocity measurements is inversely proportional to the dwell time, and is calculated using the following equation [27]:

$$\delta v \cong \frac{\Delta V}{\sqrt{2SNR}} \tag{2.36}$$

Where δv is the radial velocity measuring error. Using the same signal to noise ratio as for the range accuracy, the radial velocity measurement accuracy is estimated to be 0.05 m/s.

2.8 – Previous Work with SDA

This section will discuss the existing satellites and infrastructure in support of national SDA. Since radars are generally active sensors and suffer from a R^{-4} power loss over range, most deep space tracking

is done with optical sensors, while some LEO tracking is done with radars [29]. There are two common methods of tasking an optical sensor to track Resident Space Objects (RSOs): star stare mode (SSM) and track-rate mode (TRM) [29]. SSM is when the telescope is slewed at the same rate as the background stars, which will appear as point sources and the orbiting RSO is left to streak through the image at its current angular rate [29]. Alternatively, TRM is when the slewing rate is equal to the angular rate of the RSO making the object a point source and the stars streaks [29] .

The US SSN maintains a catalog of all known RSOs, updating their orbital parameters with observations from contributing sensors [29]. These parameters are provided worldwide in the form of TLE sets [29]. TLEs are generally accurate up to 1 km at the time they are generated and are good enough to point the antenna in the relative direction of the satellite [29]. Models of all the forces and perturbations acting on satellites that affect their projected orbital paths are incorporated into orbit calculations when tracking satellites' movements. However, these force models are not complete in representing all forces, creating a need to periodically update these estimated orbits. Some of the factors influencing object orbits include atmospheric drag and gravitational pulls from both the Earth and other nearby large bodies. Without corrections, it is found that the positional error can grow 1-3 km per day [29].

The standard analytical propagator designed for use with the TLE format is known as Simplified General Perturbations version 4 (SGP4). The SGP4 predicts the effect of perturbations caused by Earth's shape (oblate), drag, solar radiation pressure, and gravitational effects from the Sun and the Moon. Propagation models are used to predict where the found object will likely be in the future once its position and velocity has been estimated.

As mentioned previously, Canada currently has two active satellites that provide data for SDA: NEOSSat and Sapphire [2]. Both these satellites use optical systems to gather data and will be discussed in the following paragraphs.

The NEOSSat spacecraft was launched in February 2013 and orbits at an altitude of 786 km with an orbital period of approximately 100 minutes [30]. It is a microsatellite weighing only 74 kg [29] that uses a telescope to search for interior-to-Earth asteroids using both SSM and TRM [2], [29]. The NEOSSat spacecraft was deployed for two primary missions: Near Earth Space Surveillance (NESS) for asteroid detection and high Earth orbit surveillance (HEOSS) [29]. Launched into a sun-synchronous polar orbit, the NEOSSat has a continuous view of a region of the geostationary belt offering it an excellent vantage point for imaging deep space RSOs [29]. The NEOSSat also doubled as an experiment to see how viable it is to conduct space surveillance from a microsatellite platform, opening the door to more cost-effective methods to conduct space surveillance [29].

The Sapphire spacecraft is a Canadian space surveillance small satellite weighing only 150 kg launched as a secondary payload on the Polar Satellite Launch Vehicle in 2013 and orbits at an altitude of 800 km with an orbital period of approximately 100 minutes [31]. It is controlled by Department of National Defence's (DND) Sensor System Operations Centre (SSOC) and uses an optical payload for data collection [31]. This satellite was designed to monitor space debris and satellites within an orbit of 6,000 km to 40,000 km above the Earth [31]. The Sapphire satellite has been contributing to the US SSN since 2014. It is commanded to the desired orientation by the command station on ground, then a series of images are taken by the payload and telemetered back to the ground station for image data processing which include precise determination of the RSO location and trajectory with an accuracy of 6 arcseconds and a brightness range of visual Magnitudes 6 to 15 [31].

Radar Based SDA

Radar systems are employed as ground stations for commanding and controlling satellite movements in orbits. This allows governments and private companies to keep visibility on and control of their satellites but does not provide an awareness of surrounding objects [7].

In 2013 Livingstone [4] conducted a radar system study to examine system concepts at a high-level as part of a much broader option analysis activity that was conducted by the DND Surveillance-of-Space-2 project office. The intended outcome of this broader study was to determine a small set of implementable deep-space surveillance options that may be further examined as Canadian contributions to the SSN. The following four ground-based radar concepts were found financially feasible to implement with current infrastructure and technology [4]:

1) employ an existing radio telescope as a component of a bistatic radar that uses a US transmitter;
2) build a deep-space radar mode for the Algonquin radio telescope and operate it for space surveillance as a secondary mission;
3) build a dish antenna based deep space radar and operate it as dedicated space surveillance radar with deep-space capabilities; and
4) build an electronically steered beam planar array radar that would be dedicated to space surveillance activities for all satellite altitudes.

Two space-based concepts were also considered that could detect and monitor small, geosynchronous debris objects [4]:

1) build secondary sensors that can be mounted on geostationary satellites to monitor and track debris items in the local area that surrounds the satellite; and
2) build a radar space surveillance satellite that operates in a sub-geosynchronous orbit to detect and measure the orbit parameters of debris in the geosynchronous orbit belt.

Following his 2013 publication [4], scientists and engineers at DRDC have continued this research and are conducting experiments to implement the concepts discussed by Livingstone, see [5], [7], and [32].

Introducing radar sensing as a tool for SDA brings forward several advantages, especially when paired with the existing optical systems Canada has employed. Unlike optical, radar sensing makes use of radio wave rays for transmissions, which are unimpeded by clouds and unaffected by the light available [3], [5]. This would allow for continuous observation, during both day and night. When using active radar sensing, it is noted that the radar can collect the same information that optical sensors collect over a few days in only a few hours, however at a great cost to resolution [5]. Using a combined approach could counter these individual disadvantages and potentially improve Canada's SDA capabilities.

Previous Experiment with HF for SDA

Frazer et al. [28] investigated the possible use of HF radar systems to conduct line of sight space surveillance in 2013. Recall that most satellite communications are conducted on the UHF, X-, S-, Ku- and Ka-bands which range from 300 MHz to 40 GHz [11]. The HF band ranges from 3 to 30 MHz, making it an unusual frequency band to conduct space transmissions and is typically used for OTHR, which make use of the refraction properties of the ionosphere at these frequencies [12].

The qualities that allow HF waves to propagate through and refract off the ionosphere are also the properties that create limitations on their abilities to efficiently transmit using LoS. The relatively long

wavelengths and clutter from the unwanted ionospheric propagation creates higher atmospheric loss and attenuation [12], [28]. Nevertheless, if one were to operate at a high enough frequency, the ionospheric conditions can be ignored to the first order approximation and most of the wave will penetrate through the ionosphere [28].

The Australian Defence Science and Technology Group (DSTO) developed a LoS HF radar for the primary mission of conducting the investigation of man-made target scattering phenomenology [28]. As part of a system test and calibration, the research team conducted a secondary experiment to attempt to locate and track the ISS using the HF radar. The system transmitter consisted of a four-element array made of Yagi antenna elements and the receiver consisted of an array of 20 Yagi antenna elements, with one receiver per element. Standard signal processing techniques were used such as waveform pulse compression and overlapped Doppler processing [28]. The results of this experiment will be discussed in this section.

Since the size of the ISS is known, Frazer et al. [28] approximated the RCS of the ISS by estimating the satellite as an equivalent sphere of 100 m:

$$\sigma_{ISS} \cong \sigma_{100m\ sphere} \tag{2.37}$$

Using a center frequency of 30 MHz, the RCS was estimated to be approximately $\sigma_{ISS} = 39$ dBm^2, but it is stressed by the authors of [28] that this is not an accurate estimation.

Using the following energy budget equation with the known altitude and approximated RCS of the ISS, the maximum signal –to-noise ratio was estimated to be 52 dB [28]:

$$s = \frac{P_t G_t(\theta,\phi;\psi_t) G_r(\theta,\phi;\psi_r) \lambda^2 \sigma}{(4\pi)^3 kTB r_t^2 r_r^2 n_e n_i L_t L_r} \tag{2.38}$$

where the terms are defined in Table 2.3.

Table 2.3 Variable definitions for (2.38).

Parameter	Symbol	Values	Unit
Transmitted power	P_t	16	kW
Transmitted array gain (max)	G_t	37.2	Linear, no units
Received array gain (max)	G_r	134.9	Linear, no units
wavelength	λ	10	m
Target RCS	σ	7.9x10^3	m^2
Thermal noise limit	kT	5x10^{-21}	W/Hz
Processing bandwidth	B	1	Hz
Range transmitter target	r_t	548	km
Range of target receiver	r_r	548	km
External to internal noise ratio	n_e	7.9	Linear, no units
Internal noise	n_i	6.3	Linear, no units
Transmitted losses	L_t	1.12	Linear, no units
Signal processing losses	L_r	5.01	Linear, no units

In the conclusions drawn from the calculations conducted in the written report at reference [28], it was estimated that the ISS would be visible for at least a portion of its overpass. Frazer et al. [28] did not use the Doppler frequencies to calculate velocity as the measurements were ambiguous for the waveform repetition frequency that was used. However, they could have used the TLE values to resolve the ambiguity. Based on results found, it was postulated that objects in the order of 2 m in physical size may be detectable at 500 km range and objects of size 4 m may be detectable at 1000 km range [28].

One of the biggest limitations in [28] is the lack of "truth data" to compare the estimated orbit against, and therefore this experiment is unable to make a definitive claim as to whether the updated TLE is more or less accurate than that of the NORAD TLE. Since this experiment was conducted incidental to the radars main purpose as part of a system calibration and testing, no effort was put forward to request access to the ISS GPS ephemerides for comparison. Orbit determination was done using angle only data and over a short 30s window. DSTO calculated a range difference of around 4 km and a direction difference of around 0.5° between the initial and refined orbits, which seems rather large. One would expect to only see a difference of <1 km and <0.1° based on the accuracy of TLEs. A possible explanation for this large correction could be explained by ionospheric effects.

Frazer et al. [28] have shown that is it possible to detect space targets with an HF radar using 30 MHz, however they did not clearly demonstrate that the approach can give accurate orbit determination results for the observed space objects, leaving a potential area of interest which is partially explored by this research.

Chapter 3

Conducted Research

The conducted research is broken down into three phases: preliminary research, experiment development and execution, and results and validation. Each of these phases will be discussed in the following subsections.

3.1 – Phase 1 – Preliminary Research

This phase includes the discussion and analysis of the operating radar, beam forming techniques to counter mutual coupling, maximum range and unambiguous range calculations, and expected power received.

3.1.1 – HF Radar Operation

DRDC currently owns and operates two HF radars, one in Ottawa and one in the Arctic. The transmitter and receiver located in Ottawa were utilized for this research due to the accessibility to these sites.

The radar system in Ottawa consists of a 64-element monopole planar-array transmitter located at DRDC, with a receiver in Ashton, approximately 20 km away, of 256 element monopole planar-array. The transmitter has access to 1 kW of power per element. The transmitter elements are 9 m high with 8 m separation. The receiving site is slightly different, as the elements are shorter at 4.88 m high with spacing of 16 m [33]. The choice to use a 2D planar array of monopole antenna elements was guided by the simplicity of installation and the possibility to steer in any azimuth and elevation direction. Since the intent was to install the same system in the Arctic, the installation in extreme cold temperatures would be difficult, and the need to steer around aurora clutter would demand the ability to control the beam direction in both planes [33]. Although there are obvious advantages to using a 2D planar array, the operation of said arrays is far from trivial. At the installation site, the limited space precludes the use of high gain elements, which greatly increases mutual coupling in the array. This must be considered in the operation of the radar rather than in the design process.

Antenna Configuration

The total field of an array is equal to the field of a single element positioned at the origin multiplied by a factor widely known as the array factor (AF) [34]. The AF is a function of the geometry of the array and the excitation phase and amplitude. By varying the separation, amplitude and/or phase between the elements, one can control the total field of the array.

Using FEKO simulation software, Figure 3.1 shows a model of a single monopole element of both the transmitter (left) and the receiver (right), over a ground plane at 20 MHz. To simulate ground, a dielectric substrate using the conductivity of $1x10^{-3}$ S/m and relative permittivity of 10 F/m was added to create a ground plane in FEKO that simulates earth [35]. Using this and an AF, the expected radiation pattern of each element can be estimated.

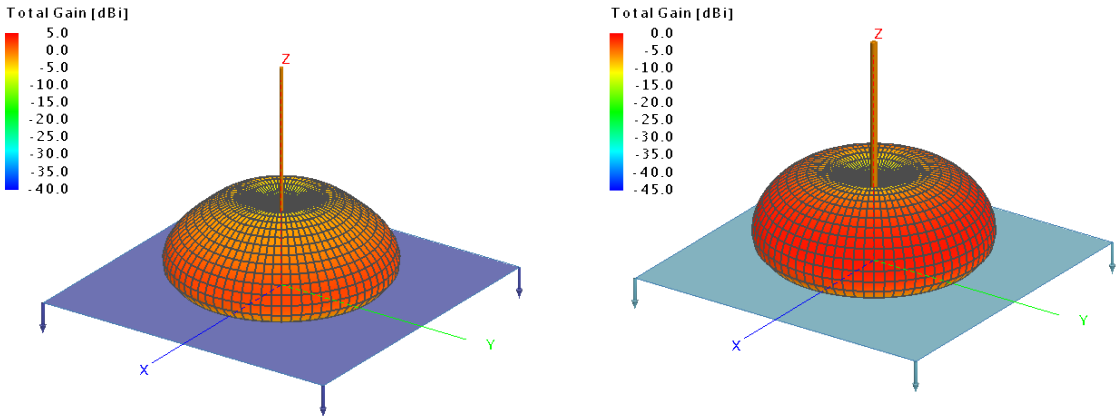

Figure 3.1 Transmitter (left) and receiver (right) single monopole elements radiation patterns over ground.

However, the actual radar configuration has radial wires in the ground [33], therefore providing a metallic component. As such, using a PEC to simulate the ground may be more accurate than using earth. This is modelled in Figure 3.2. This will be less accurate at lower elevation angles due to the reflections caused by the ground, however, for this experiment lower elevation angles could not be used due to propagation restrictions with HF waves. Therefore, using PEC for simulations will provide an accurate enough estimation.

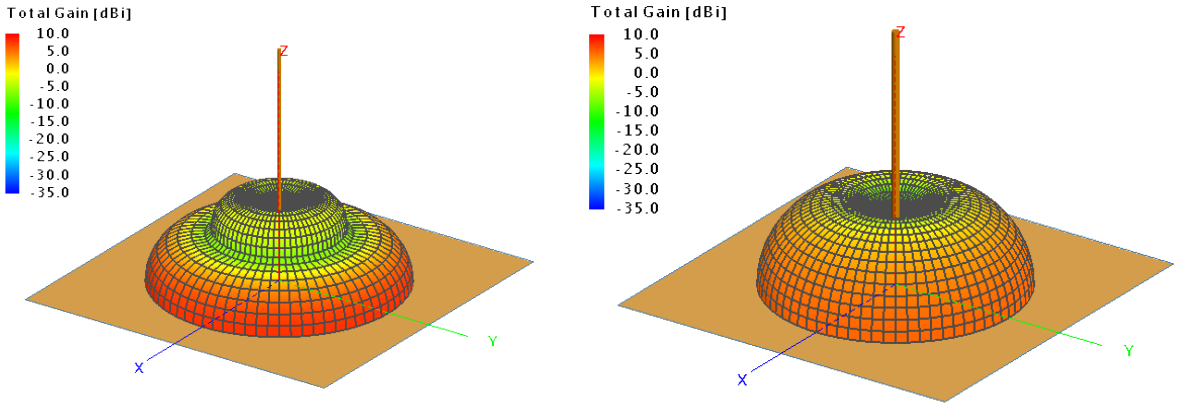

Figure 3.2 Transmitter (left) and receiver (right) element over PEC.

The array factor for the entire 2D rectangular array with uniform amplitude, linear phase progression, and equally spaced can be written as [34]:

$$AF_n(\theta,\phi) = \left\{\frac{1}{M}\frac{\sin(\frac{M}{2}\psi_x)}{\sin(\frac{\psi_x}{2})}\right\}\left\{\frac{1}{N}\frac{\sin(\frac{N}{2}\psi_y)}{\sin(\frac{\psi_y}{2})}\right\} \tag{3.1}$$

where

$$\psi_x = kd_x \sin\theta \cos\phi + \beta_x$$
$$\psi_y = kd_y \sin\theta \sin\phi + \beta_y$$

The variables found in (3.1) are defined in Table 3.1.

Table 3.1 Variable definitions for (3.1).

Variable symbol	Variable name
$\boldsymbol{m}$	The element position in the x-direction
$\boldsymbol{M}$	Number of elements in the x-direction
$\boldsymbol{n}$	The element position in the y-direction
$\boldsymbol{N}$	Number of elements in y-direction
$\boldsymbol{k}$	$2\pi/\lambda$
$\boldsymbol{d_x}$	Element spacing in the x-direction (meters)
$\boldsymbol{d_y}$	Element spacing in the y-direction (meters)
$\boldsymbol{\theta}$	Elevation angle (radians)
$\boldsymbol{\phi}$	Azimuth angle (radians)
$\boldsymbol{\beta_x}$	Progressive phase shift of the elements in the x-direction (radians)
$\boldsymbol{\beta_y}$	Progressive phase shift of elements in the y-direction (radians)

Solving for the array factor to estimate the final radiation pattern theoretically does not consider mutual coupling between the elements. The only way to ensure this is fully considered is to calculate the radiation pattern of each element in the presence of the other elements. This is easiest to do with a simulation tool such as FEKO, as modelled in Figure 3.3.

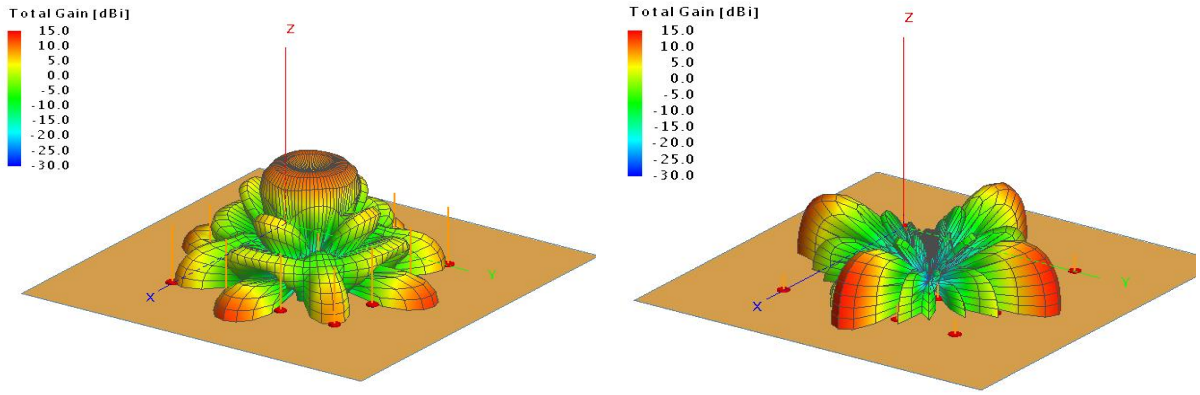

Figure 3.3 4x4 array (smaller versions of the actual arrays) left transmitter, right receiver.

Figure 3.3 above represents the expected radiation pattern of both the receiver and the transmitter in the presence of the other elements, with no phase shifts and separation between elements of 8 m for the transmitter and 16 m for the receiver. The transmitting array, when there are no phase shifts present, has a large main lobe with a gain of up to 15 dBi, but has many side lobes.

Beam Forming

The OTHR system at DRDC can be modeled using an equivalent circuit with a voltage source in series with a generator impedance of 200 Ohms (Z_G) and a perfectly matched antenna input impedance of 200 Ohms (Z), as seen in Figure 3.5. For transmission, each element is capable of transmitting 1 kW of radiated power, however due to losses in the circuit, 2 kW of power will be provided to ensure the element receives the full 1 kW. Using the following equation, the required voltage to achieve these parameters can be calculated:

$$P = \frac{V^2}{2R} \tag{3.2}$$

Using the known values, the correct voltage of 1264.91 V can be calculated to achieve the desired results.

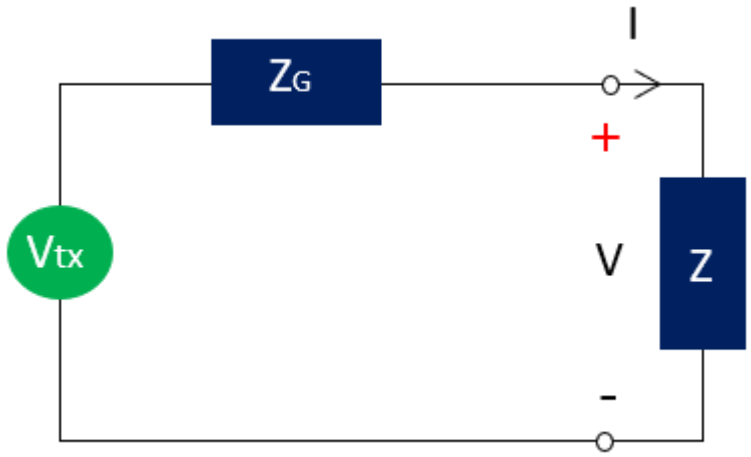

Figure 3.4 Circuit equivalent for radar transmit array.

The transmit array can be represented by the equivalent circuit seen above in Figure 3.4. Feed currents for each array element are given by the following column vector of P rows [33]:

$$I = (Z_G + Z)^{-1} v_{tx} \tag{3.3}$$

where P is the number of elements, Z is the array mutual impedance matrix, Z_G is a diagonal matrix of the generator impedances connected to the array elements, and v_{tx} is a column vector containing the generator voltages. This can be related to the forward voltage (v^+) with the following relationship:

$$v^+ = \frac{v_{tx}}{2} \tag{3.4}$$

Forward voltage is defined as forward travelling waves. The high level of mutual coupling that is expected will affect the impedance matching, causing signal reflections to occur. These can be represented by:

$$v^- = S v^+ \tag{3.5}$$

where $S = (Z + Z_G)^{-1}(Z - Z_G)$.

To steer the beam in a desired direction, there are two approaches that can be considered. First, using beamforming weights to the currents applied to each element, using equation (3.3) or second, using beam forming weights applied to the forward voltages seen in equation (3.4). As seen in [33], by using the feed current method, the voltages must be normalized due to mutual coupling, therefore resulting in underutilization of transmitter resources. For the forward voltage beamforming, all the transmitter resources are used, but there will be strong reflected signals, especially in such a highly coupled system as this one. Depending on the high-power amplifiers, this means there may need to be additional backoff required.

Based on the analysis conducted in ref [33], the feed current beamforming approach produced low radiated power that rarely exceeded 100 kW due to the requirement to significantly reduce voltage

amplitudes to normalize them with respect to the element with the strongest power level. However, the forward voltage beamforming method produced much more promising results and provides much higher power levels, in some areas up to 220 kW. With this method there exists strong reverse power levels of up to 1000 W that will be require additional backoff, as the 3 dB uniform backoff recommended by the High Power Amplifier (HPA) will not be sufficient. To counter this, a non-uniform backoff using an iterative procedure was implemented [33].

For this experiment the same process as discussed in [33] was implemented to achieve the maximum transmission effectiveness.

Received Power

Since the radar beam will be moving to different azimuth and elevation angles to follow the satellite throughout its orbit, the power levels will fluctuate as the gain value changes. The expected power will therefore need to be calculated over the orbit duration at all azimuth and elevations to ensure detection. For this estimation, the gain values at elevations 5° to 90° and azimuths -180° to 180° in 5° increments were simulated with FEKO software.

Realized gain is more valuable to use in these estimations as it is dependent on the impedance mismatch loss from the system. This can be modeled with the following equation:

$$G_{realized} = (1 - |\Gamma|^2)G \tag{3.6}$$

where Γ is the reflection coefficient of the system and G is the absolute gain. The transmitted power (for the research 64 kW or 48 dBW was used) subtracted from the Equivalent isotropic radiated power (*EIRP*) will provide an accurate estimate of the realized gain. The *EIRP* was estimated using FEKO software. This is modeled in equation (3.7):

$$EIRP = P_t - L_c + G_T \text{ (dBi)} \tag{3.7}$$

where P_t is the output power of the transmitter in dBm, L_c is the cable loss in dB, and G_T is the transmitter antenna gain and G_R is the receiver antenna gain in dBi.

Using antenna simulation software and MATLAB, the EIRP and the Rx antenna gain at 20 MHz was simulated and the following Figure 3.5 shows the results that were produced at elevations from 5 to 90 degrees.

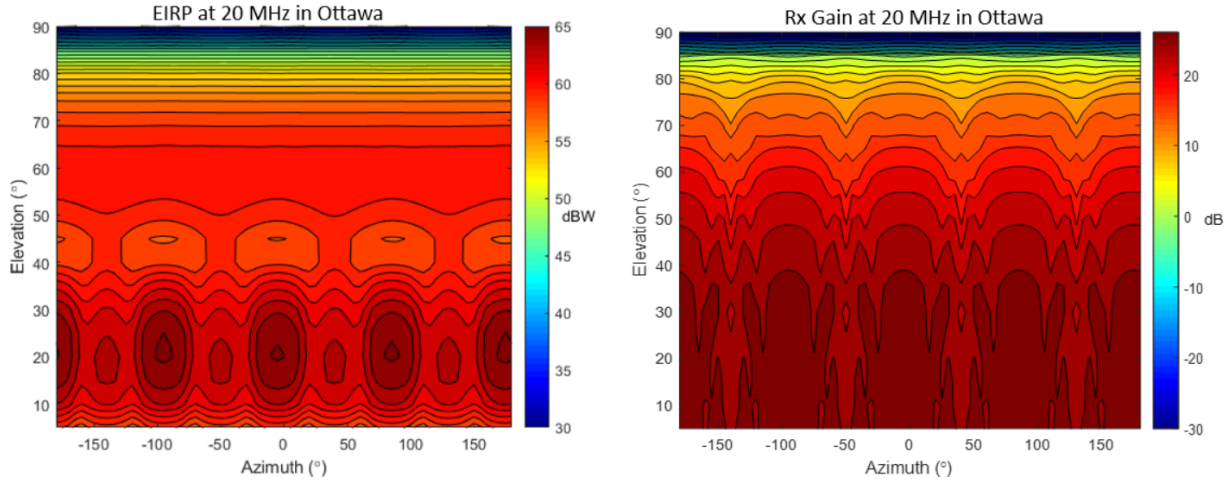

Figure 3.5 EIRP and Rx antenna gain at 20 MHz at elevations from 5 to 90 degrees. Image provided by Dr. Henault.

For an accurate calculation of received power, the EIRP can be substituted into the radar range equation for transmitted power. The equation would be modified as follows:

$$P_r = EIRP \times \frac{1}{(4\pi R^2)^2} \times \frac{\lambda^2}{4\pi} G_R \times \sigma \tag{3.8}$$

Figure 3.6 represents the received power estimation using the predicted the azimuth and elevations of the ISS during four 11 minutes passes, with a CPI of 1s, and the expected EIRP and Rx gain from Figure 3.5 at the azimuth and elevations of the predicted orbit. The red dashed line represents the noise floor determined by [16] for rural areas. As per Figure 3.6, theoretically the received power is over the noise floor for most of the passes and therefore the ISS should be visible using the radar system and operating parameters selected.

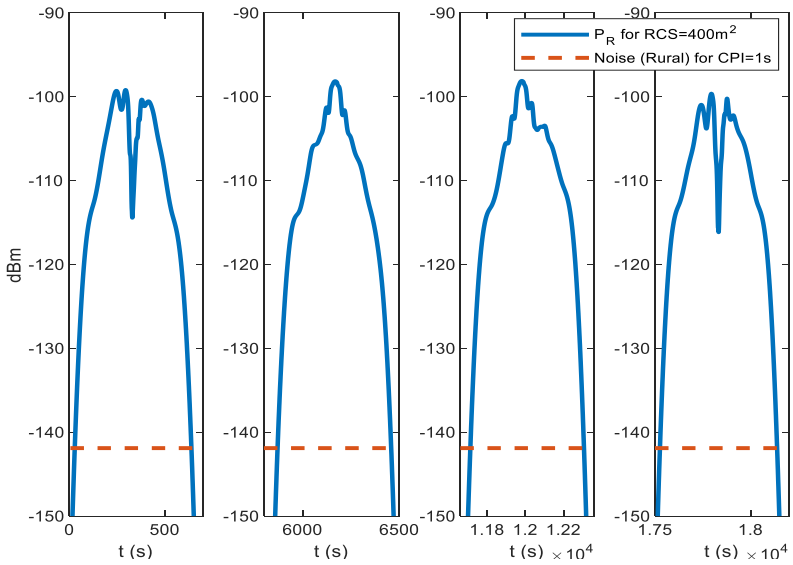

Figure 3.6 Estimated received power at 20 MHz, provided by Dr. Henault.

.

3.2 Phase 2 – Experiment Development and Execution

Phase two includes the development and employment of the signal processing algorithms on the recorded data. Data was collected over three different periods. The first collection occurred on 3 Nov 2022 using three different frequency shifts centered around 13.1174 MHz. The intent of these shifts was to validate the first order approximation of TEC measurement using the dual frequency method from [18]. Only one pass was recorded. The second set of data was observed on 11 Nov 2022, overnight, using only one frequency of 20.9015 MHz. A total of four passes were successfully recorded. The final collection time was 9 Feb 2023 during the day, using only 20.9015 MHz again. Only three of the four passes were successfully recorded due to receiver errors.

3.2.1 – Signal Processing

Range and Doppler Calculations

To track the satellite, the range-Doppler map was created for each coherent processing interval (CPI), like that done by DSTO in [28]. For this research, a CPI of 1 second was used with a typical LFMCW chirped radar signal with a bandwidth (B) of 10 kHz. Due to the hypersonic characteristics of the target, the CPI will be restricted to avoid range and Doppler migration. The equation to generate a range-Doppler map is modeled here:

$$x_n(\tau, f_D) = \sum_{i=1}^{CPI \times f_{prf}} e^{-j2\pi f_D t_i} \int_{t=0}^{1/f_{prf}} s(t) x_{ni}^*(t+\tau) dt \quad (3.9)$$

$$s(t) = e^{j\pi B f_{prf}(t - \frac{1}{2f_{prf}})^2} \quad (3.10)$$

where f_{prf} is the pulse repetition frequency (PRF), $s(t)$ is a typical LFMCW chirped radar signal with bandwidth B. This equation represents a convolution of every pulse followed by a two-dimensional discrete Fourier transform (FT) across the pulses. x_{ni}^* is the complex conjugate of the sampled data at interval i. The time delay (τ) will be estimated and will translate to range using the following relationship (bistatic) $R = c\tau = 150000\tau$ km and the Doppler frequency f_D will be estimated by locating the peak level in every range-Doppler map during the entire pass. Faraday rotation may cause the signal level to fluctuate significantly during the pass, but there should be peaks when the signal is vertically polarized.

Figure 3.7 describes the range-Doppler map produced for one CPI of one pass on 11 Nov 2022 at 07:56 UTC. The red circle indicates the predicted location of the ISS at that epoch and the small green circle indicates the measured position of the ISS. There are clutter returns visible at several ranges near zero Doppler and are due to range sidelobes from the direct transmitter to receiver signal and close-to-the-direct-signal clutter.

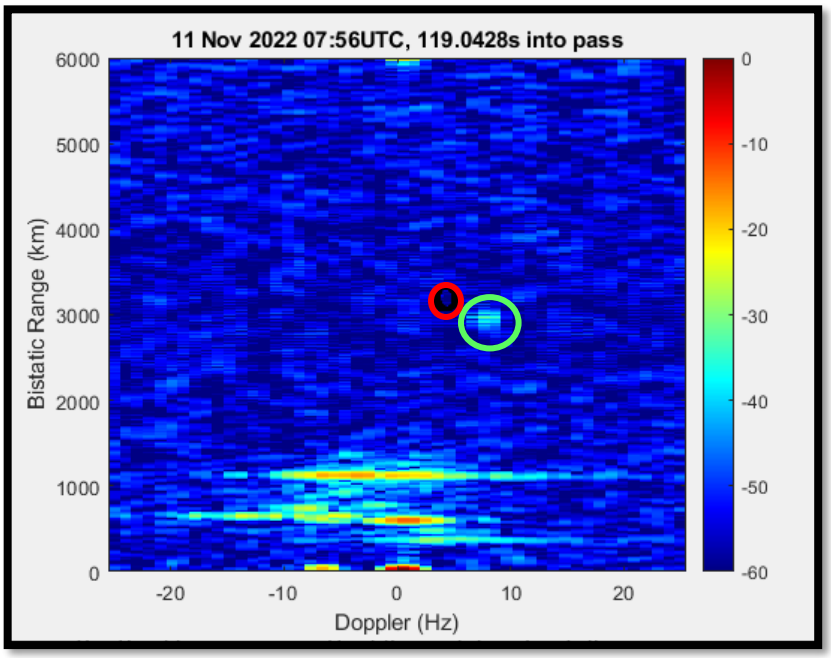

Figure 3.7 Doppler-range map produced for 1 CPI of 11 Nov pass from 7:56UTC to 8:07UTC, ISS measured location shown by a green circle, predicted TLE location shown by a red circle.

By locating the index of the maximum value in the predicted region of the ISS, the range and Doppler measurements were collected. They were then compared to the TLE predictions to determine a level of accuracy.

Using the PRF of 50 Hz, the unambiguous Doppler range will be *-PRF/2* to *+PRF/2*. However, due to the hypersonic speed of the ISS, it is expected that the Doppler measurements will be ambiguous. Using TLEs, the ambiguity can be removed from the Doppler measurements using the following relationship:

$$f_{d_a} = f_d - k_a PRF \quad (3.11)$$

Where f_{d_a} is the ambiguous Doppler frequency, f_d is the Doppler frequency and k_a is the integer such that f_d is between $-PRF/2$ and $PRF/2$. Using an iterative process, and the expected Doppler frequency from the TLE values, the k_a value can be estimated such that the residuals between f_{d_a} and f_d are minimized.

Range Compensation and Correction

Once the measured range and unambiguous Doppler frequencies are collected, error correction and compensation for range delays need to be applied to account for the multiple sources of errors within the system. Figure 3.8 shows the flow chart of how corrections will be applied to the received frequencies.

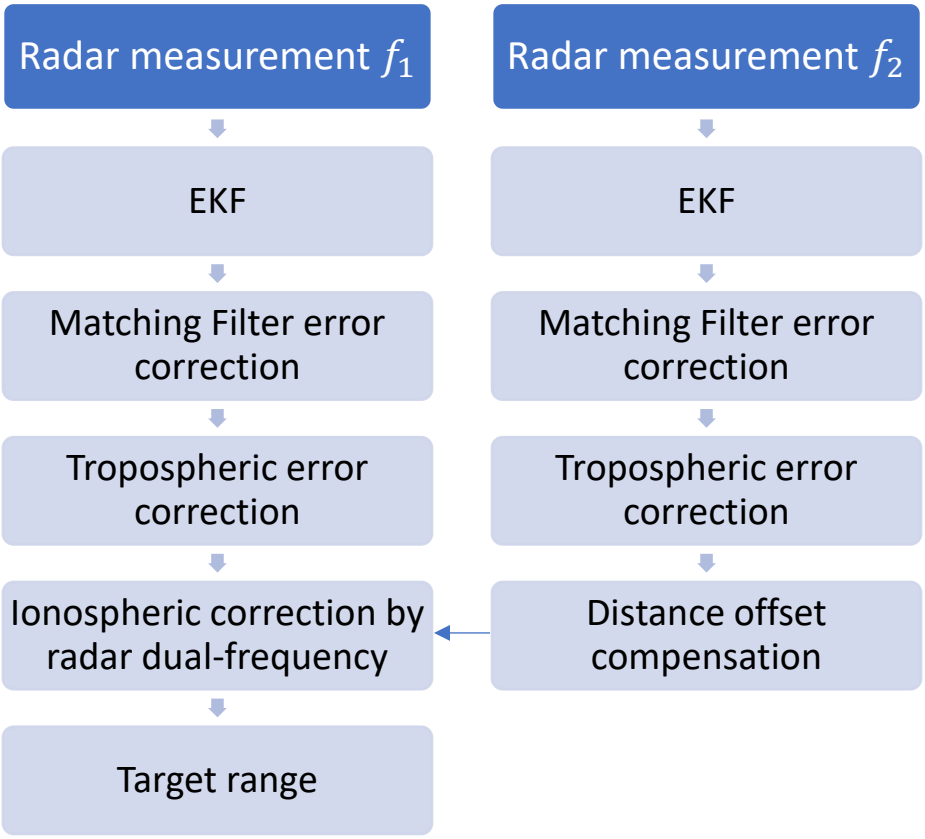

Figure 3.8 Flow chart for error compensation and correction, re-created from [18].

Each of the steps shown in Figure 3.8 will be described in the following paragraphs. The matching filter error correction and distance offset were discussed in the earlier section *2.4 Ionospheric Corrections.*

Kalman Filters for Smoothing and Predictions

The first step in error compensation and correction is to apply an Extended Kalman Filter (EKF). For the dual frequency first order validation experiment, this step is applied to both radar measurements for both frequencies being used.

Two Kalman filters were used in this experiment; one for smoothing the range using Doppler speed measurements, and the other for position prediction using measured Doppler and range.

The first Kalman filter is a simple filter that estimated the next range position using the measured filtered Doppler speed from the previous sample. The following parameters were used for the first Kalman Filter, assuming uncorrelated noise:

$$\vec{x}_k = \begin{bmatrix} r_k \\ v_{fd_k} \end{bmatrix} \tag{3.19}$$

where $r_k$is the range and v_{fd_k} is the Doppler speed at epoch k. These make up the states $\vec{x}_k$. Using the state transition matrix ϕ_k, the states at epoch k+1 can be predicted:

$$\vec{x}_{k+1} = \phi_k \vec{x}_k = \begin{bmatrix} 1 & \Delta t \\ 0 & 1 \end{bmatrix} \begin{bmatrix} r_k \\ v_{fd_k} \end{bmatrix} \tag{3.20}$$

With the following measurement matrix H:

$$H\vec{x}_k = \begin{bmatrix} 1 & 0 \\ 0 & 1 \end{bmatrix} \begin{bmatrix} r_k \\ v_{fd_k} \end{bmatrix} \tag{3.21}$$

This filter removed some of the major outlier points, increasing the overall accuracy of the measurements and is applied at the first step of the signal processing process.

The second Kalman Filter that was applied was to estimate the position and smooth the estimates of the ISS using only the Doppler and range measurements. The filter is defined as follows:

$$\vec{x}_k = \begin{bmatrix} r_k \\ \dot{r}_k \\ f_{D_k} \\ \dot{f}_{D_k} \end{bmatrix} \tag{3.22}$$

where the state matrix at epoch is made of the measured range r_k, the time derivative of the measured range $\dot{r}_k$ (constant velocity of the target), the measured Doppler frequency f_{D_k}, and the time derivative of the measured Doppler frequency $\dot{f}_{D_k}$. Using the following transition rules:

$$r_{k+1} = r_k + \dot{r}_k \Delta t \tag{3.23}$$

$$\dot{r}_{k+1} = \dot{r}_k \tag{3.24}$$

$$f_{D_{k+1}} = f_{D_k} + \dot{f}_k \Delta t \tag{3.25}$$

$$\dot{f}_{D_{k+1}} = \dot{f}_{D_k} \tag{3.26}$$

and the following relationships are true:

$$\dot{r}_k = (r_{k-1} - r_k)\Delta t \tag{3.27}$$

$$\dot{f}_k = (f_{D_k} - f_{D_{k-1}})\Delta t \tag{3.28}$$

$$\vec{x}_{k+1} = \phi_k \vec{x}_k = \begin{bmatrix} 1 & \Delta t & 0 & 0 \\ 0 & 1 & 0 & 0 \\ 0 & 0 & 1 & \Delta t \\ 0 & 0 & 0 & 1 \end{bmatrix} \begin{bmatrix} r_k \\ \dot{r}_k \\ f_{D_k} \\ \dot{f}_{D_k} \end{bmatrix} \tag{3.29}$$

$$H\vec{x}_k = \begin{bmatrix} 1 & 0 & 0 & 0 \\ 0 & 0 & 1 & 0 \end{bmatrix} \begin{bmatrix} r_k \\ \dot{r}_k \\ f_{D_k} \\ \dot{f}_{D_k} \end{bmatrix} \tag{3.30}$$

This second filter will be applied at the end of the process to attempt to smooth the curve more accurately.

Atmospheric Correction Methods

As mentioned previously in section *2.4 Ionospheric Corrections*, the TEC along the path of propagation will be estimated using phase shifts of received pulses from two different frequencies. This will be compared to TEC calculated using PHaRLAP.

PHaRLAP which uses the International Reference Ionosphere (IRI) 2016 model to generate the ionosphere model. The IRI 2016 is an international ionospheric empirical model that is used worldwide. It is based on a large amount of ground-based and space-based observational data, mainly from satellites, incoherent scattering radars, and altimeters [36].

The elevations and azimuths from the TLE predictions were used to ray trace the propagation path and estimate the TEC for each second of transmission. Figure 3.9 is an example of some of the traced rays of the transmission path.

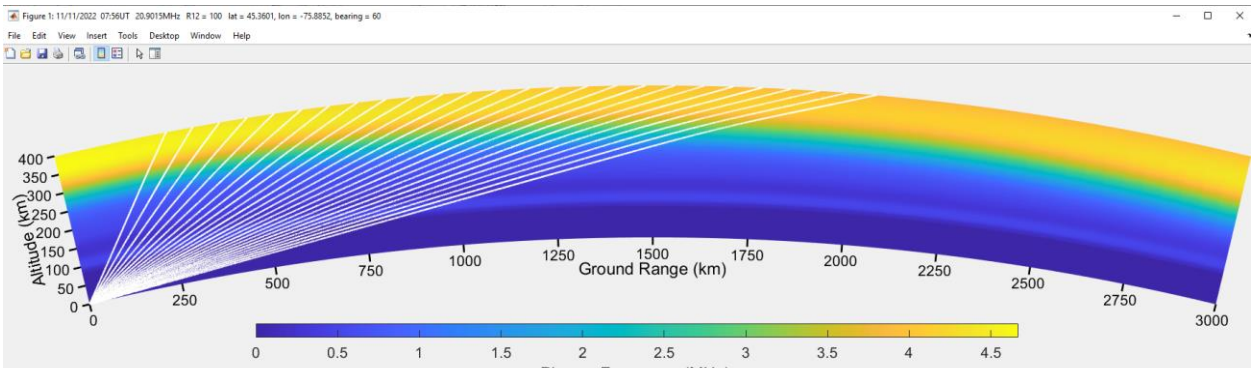

Figure 3.9 Ray tracing using PHaRLAP program for each elevation and azimuth angle during ISS TLE pass 11 Nov 2022.

Using this software, the TEC along the propagation path is estimated for each elevation and azimuth angle provided by the TLE predictions of an entire pass over the receiver site. Using the previously derived equation (2.7), the range delay from the ionosphere can be estimated.

Since the transmission will be two ways, the delay will be doubled to account for both trips through the ionosphere. To account for the 20 km distance between the transmitter and receiver and for higher accuracy in measurements, rays can be traced from both locations instead of simply doubling the transmitted estimation.

Using the 3 Nov 2022 transmission of three different frequency shifts, each frequency was processed as a separate signal to identify the different phase shifts of the received signals for comparison and estimation of TEC, as described in section *2.4 Ionospheric Corrections*.

The errors caused by the troposphere will also be accounted for using a MATLAB program provided and developed by Dr. Malek Karaim from the RMC Navigation Research Group. This program uses a vector of elevation angles (degrees) for the visible satellite, the receiver geodetic height (m), the

receiver latitude and the relative humidity from 0-100 to estimate the range delay (m). These estimated range delay errors are not frequency dependent but are affected by air humidity, temperature and pressure, therefore time of year and weather will be a factor when estimating the tropospheric corrections. Using online weather prediction sites, the following humidity levels were used for the recorded transmissions [1]:

Table 3.2 Humidity levels for each transmission time [1].

Date-Time (UTC)	Humidity (%)
3 Nov 22 – 11:08:50	95
11 Nov 22 – 03:05:00	45
11 Nov 22 – 04:42:00	64
11 Nov 22 – 06:19:00	68
11 Nov 22 – 07:56:00	81
9 Feb 23 – 15:38:00	94
9 Feb 23 – 17:16:00	96
9 Feb 23 – 20:30:00	94

The ionospheric Doppler errors were estimated using the PHaRLAP predicted TECs and phase paths for each pass. Two different methods were compared, the first method uses the time derivative of the TEC values to estimate the frequency shift caused by the Ionosphere. The second method will use the time derivative of the phase path error.

3.3 – Results and Validation

This section will discuss the results produced from the signal processing techniques introduced in the previous section, as well as provide standards of validation to determine if HF transmissions is feasible to conduct accurate SDA.

3.3.1 – Results

Figure 3.10 shows one CPI (1 s) of each transmission conducted for this experiment. Figure 3.10 (a) shows the range-Doppler plot for the dual frequency validation test on 3 November 2022, using the lower frequency of 13 MHz. In this map there is some ground clutter as well as other clutter and noise caused by the atmospheric effects due to the use of a lower frequency within the HF band. The ISS is sporadically visible in very short bursts throughout the pass, never long enough to collect accurate measurements. Using a transmitting frequency of 20 MHz, a night transmission period on 11 November 2022 and a day transmission period on 9 February 2023 were also conducted to compare the effectiveness of HF during different times of solar activity. Each transmission period attempted to collect data over 4 different passes; the night time period successfully collecting data from 4 out of the 4 measured passes, and the day time period successfully collecting data from 3 out of the 4 measured passes. Figure 3.10 (b) shows a range-Doppler map for the fourth pass from the night transmission period on 11 Nov 2022, and (c) is the map for the fourth pass from the day transmission period on 9 Feb 2023. There is clearly a higher level of ground clutter present during the day time transmission, shown around the 0 Doppler area caused by skywaves. The ISS is only visible for a short duration during the pass, approximately 100 seconds. The night pass has much less clutter and a longer visibility period of 440 seconds.

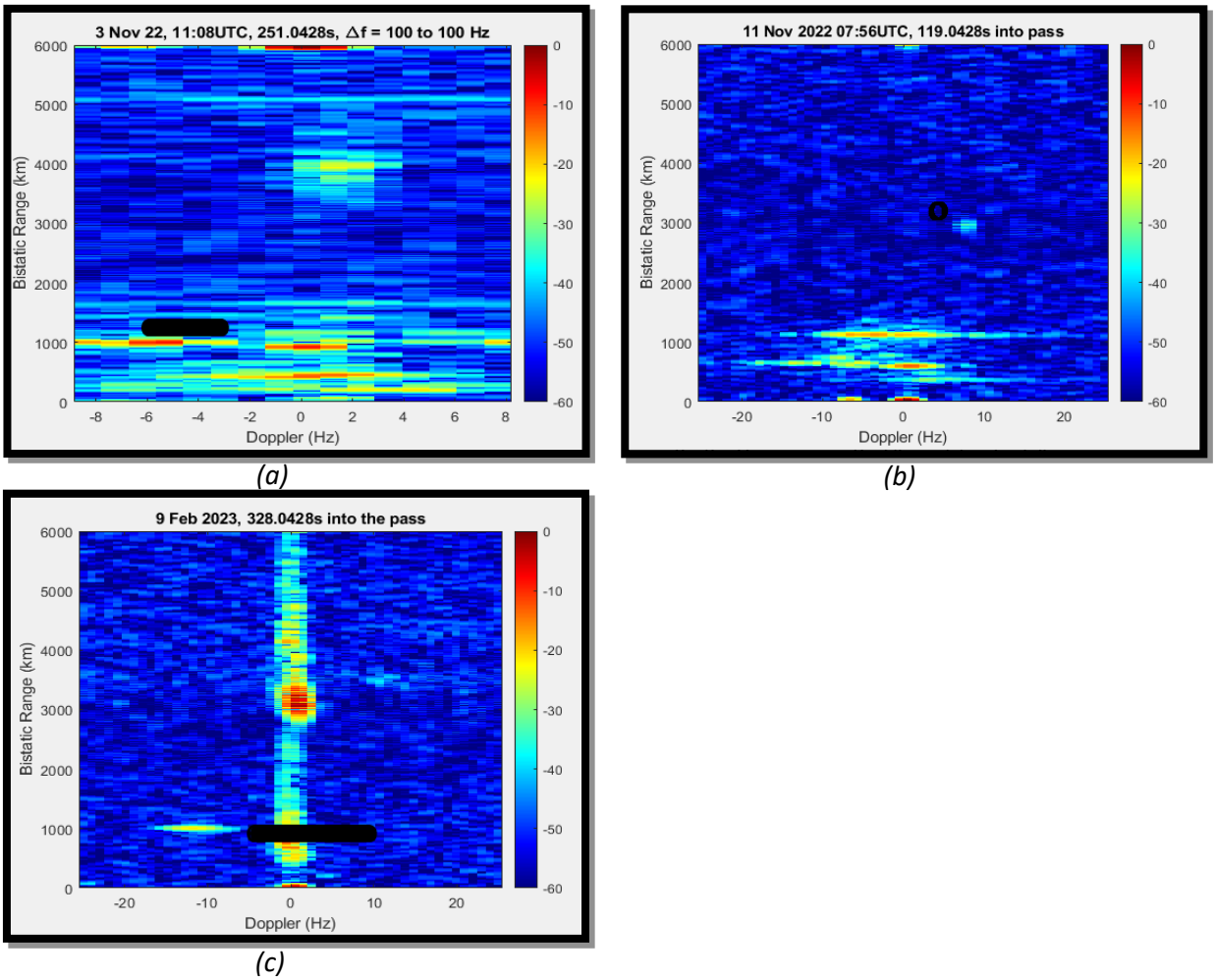

Figure 3.10 Range Doppler maps for transmissions on (a) 3 Nov 22 - dual frequency, (b) 11 Nov 22 - night time, (c) 9 Feb 23 - Day time. TLE predictions shown in black.

The following sub-sections will discuss the results from the signal processing for the fourth pass conducted during the night transmission period on 11 Nov 2022 and the fourth pass during the day transmission period on 9 Feb 2023. The transmission on 3 Nov 2022 will not be discussed in great detail due to the lack of useable data for processing.

It is important to note that for the range diagrams shown below in the next sub-sections, the maximum values of the Doppler-range maps were collected using a changing filter that only considered up to a maximum distance of ± 600 km from the predicted TLE range depending on epoch of the pass. This was done to avoid the direct signal clutter that appears at the 0 Doppler and 20 km position, representing the direct link between the transmitter and receiver.

Measurements and Residuals

The following Figures 3.11 and 3.13 show the initial range (a) and Doppler (b) measurements of one pass from each transmission period and their residuals (c) compared to the predicted TLE measurements, before any corrections were applied. The low PRF of 50 Hz created ambiguous Doppler measurements, however, with the use of the TLEs, the ambiguity can be removed using the process described earlier in section *3.2.1 Signal Processing*. The Doppler frequencies shown below in the

following figures compare the measured data to the predicted Doppler after ambiguity is removed. This creates wrapped errors bounded by *-PRF/2* and *PRF/2* that were unwrapped for error analysis.

The Figure 3.11 (a), (b) and (c) show the night transmission measured range, Doppler and associated residuals. The ISS is clearly visible for most of the pass with the exception of the very beginning and end when the elevation angles were the lowest. Visible portion is boxed in green.

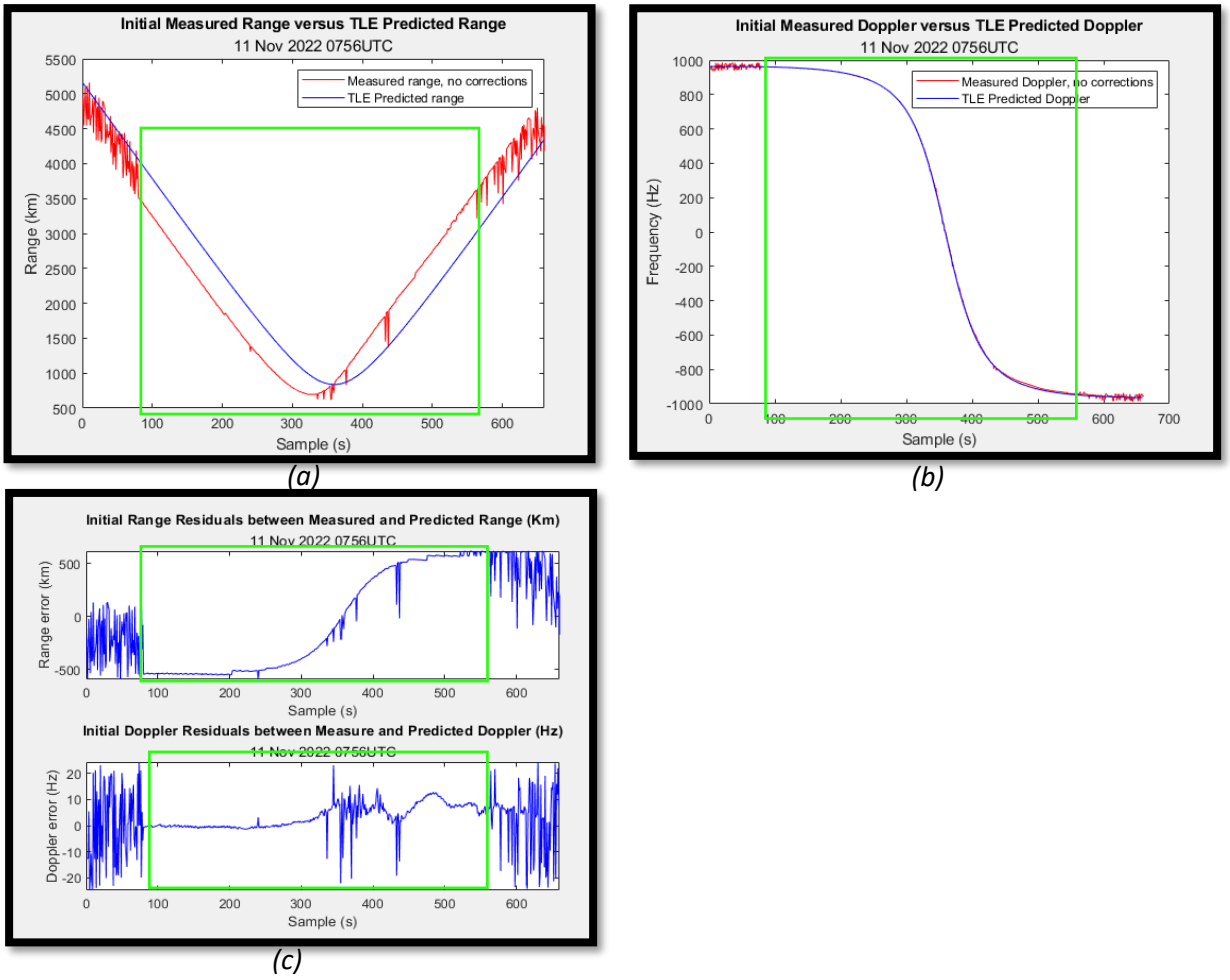

Figure 3.11 11 Nov 2022 night transmission with visible portion boxed in green (a) Initial measured ranges shown in red and Predicted Ranges shown in blue, (b) Initial measured Doppler shown in red and predicted Doppler shown in blue, (c) associated residuals.

The ISS is visible during this pass from approximately the 100 s mark until 540 s. The higher noise presence at the lower elevations is likely due to the qualities of HF skywave propagation where the angle of transmission was below the critical angle for piercing the atmosphere, or the ISS was hidden in the ground clutter. Figure 3.12 shows the elevation during the entire pass for the fourth pass on 11 Nov 22 transmission. The areas where the ISS is not visible occurs when the ISS is below 10°.

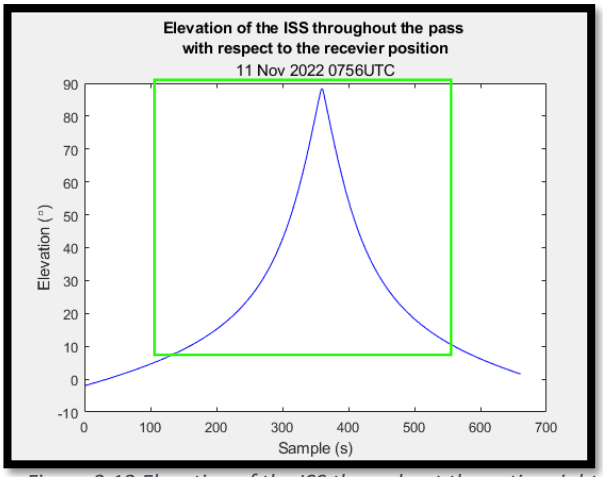

Figure 3.12 Elevation of the ISS throughout the entire night pass with respect to the receiver site, 11 Nov 2022. Visible portion boxed in green.

Figure 3.13 (a), (b) and (c) show the results from the selected day transmission on 9 Feb 23. These measurements show a much higher level of clutter present concealing the ISS except for the 100 s period where the ISS is visible between the 275 s and 375 s mark, shown by a red box. This is likely due the higher solar radiation in the ionosphere causing higher levels of attenuation and refraction. At the zero Doppler position there is higher levels of ground clutter caused by skywaves refracting off the more ionized atmosphere. The period of visibility is when the ISS is closest to the receiver.

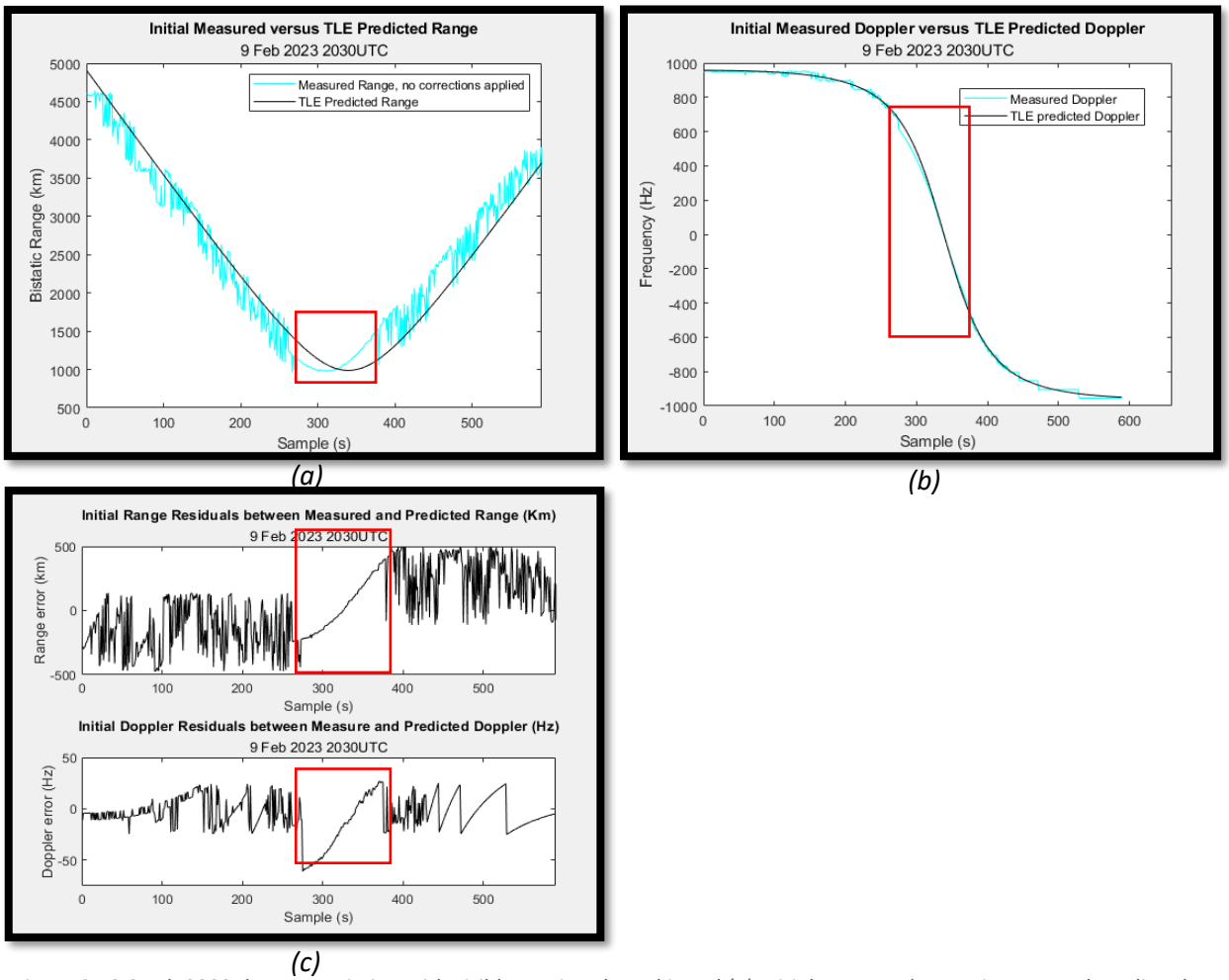

Figure 3.13 9 Feb 2023 day transmission with visible portions boxed in red (a) Initial measured range in cyan and predicted ranges in black, (b) Initial measured Doppler in cyan and predicted Doppler in black, (c) associated residuals.

Figure 3.14 shows the elevation throughout the selected day pass with respect to the receiver, the visible portion is boxed in red. The ISS is visible when the elevation is above 30° up to 60° and at the points closest to the receiver.

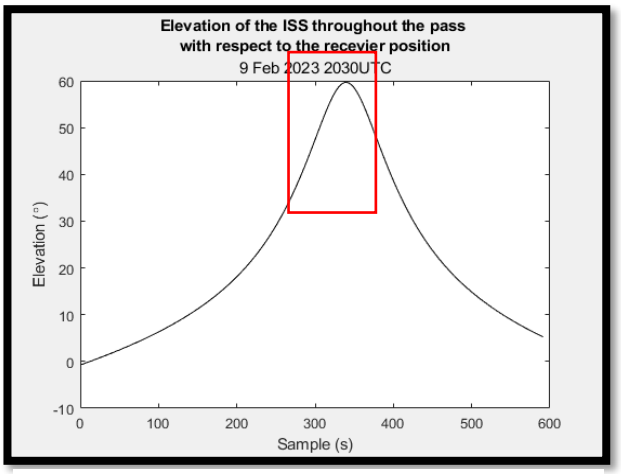

Figure 3.14 Elevation of the ISS throughout the entire day pass with respect to the receiver site, 9 Feb 2023. Visible portion boxed in red.

The Figures 3.15 and 3.16 shows the final range and Doppler measurements after the corrections were applied as per the flow chart shown above in Figure 3.8 with their corresponding range residuals and RMSE for each range correction step. The RMSE was calculated only for the period of the pass where the ISS is visible. The flow charts steps are numbered as follows:

1. Initial Kalman Filter;
2. Matching filter error correction;
3. Tropospheric error correction;
4. Ionospheric error correction;
5. Final Kalman Filter; and
6. Final target range.

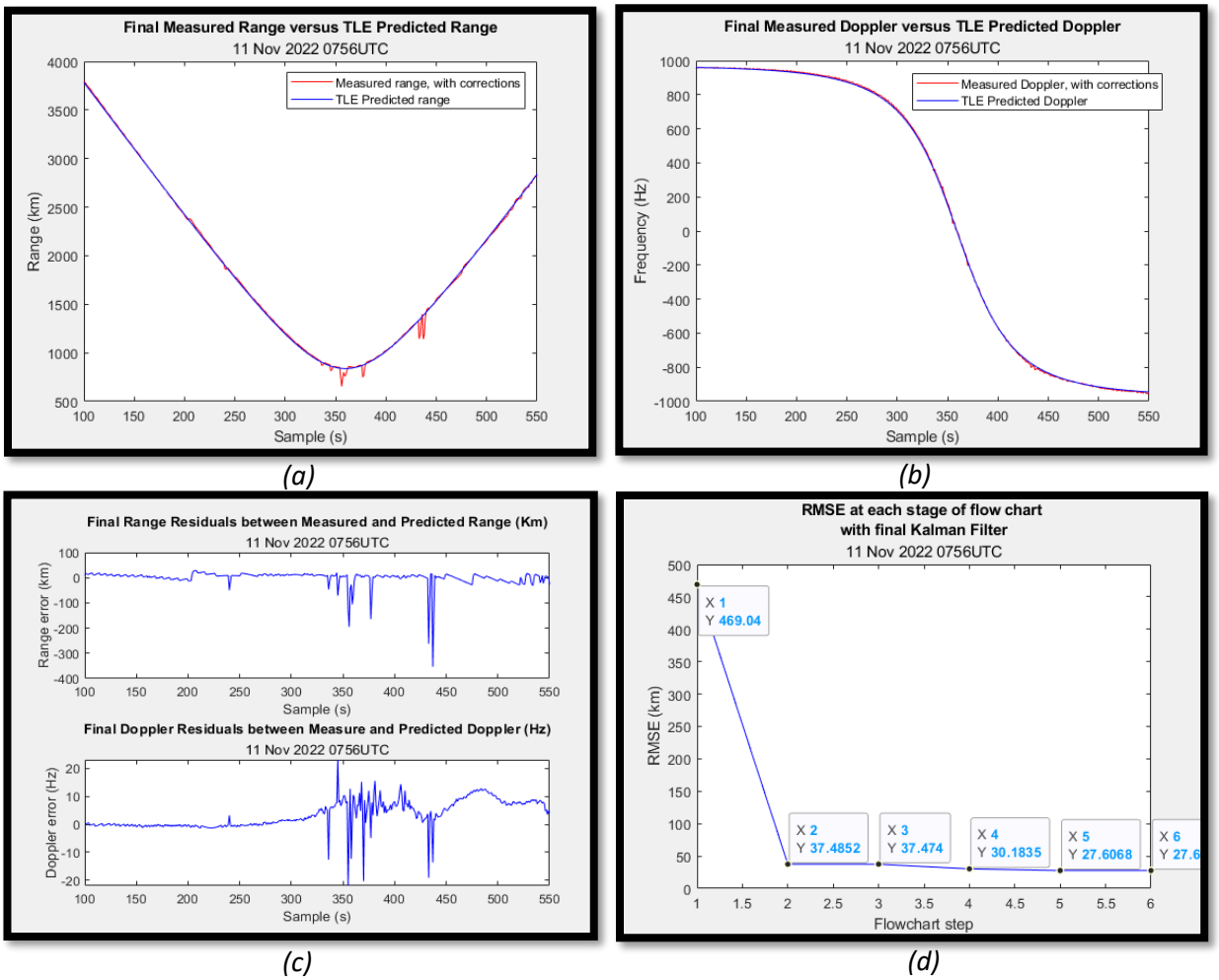

Figure 3.15 Transmission measurements 11 Nov 2022, (a) Final measured range in red versus TLE predicted range in blue, (b) Final measured Doppler in red versus TLE predicted Doppler, (c) range and Doppler residuals against TLE predictions, (d) RMSE for each range correction step: 1. Initial Kalman Filter, 2. Matching filter error correction, 3. Tropospheric error correction, 4. Ionospheric error correction, 5. Final Kalman filter, 6. Final target range.

The final estimated ranges for the night pass had a RMSE of 27.6 km and Doppler frequency RMSE of 5.97 Hz. The only notable correction made during the night pass is attributed to the matched filter correction. The biggest advantages to the night time data was the ability to locate the ISS for the majority of the pass, and the very accurate Doppler measurements. The biggest disadvantage is the overestimated TEC, causing over correction errors in the Doppler measurements. This is discussed in the following sections.

The final measurements for the selected day time transmission are shown in Figure 3.16. When comparing the night transmission measurements to the day transmission measured, there is a higher level of noise and clutter seen throughout the entire pass due to skywave propagation caused by the higher TEC, limiting time on target to only 100s.

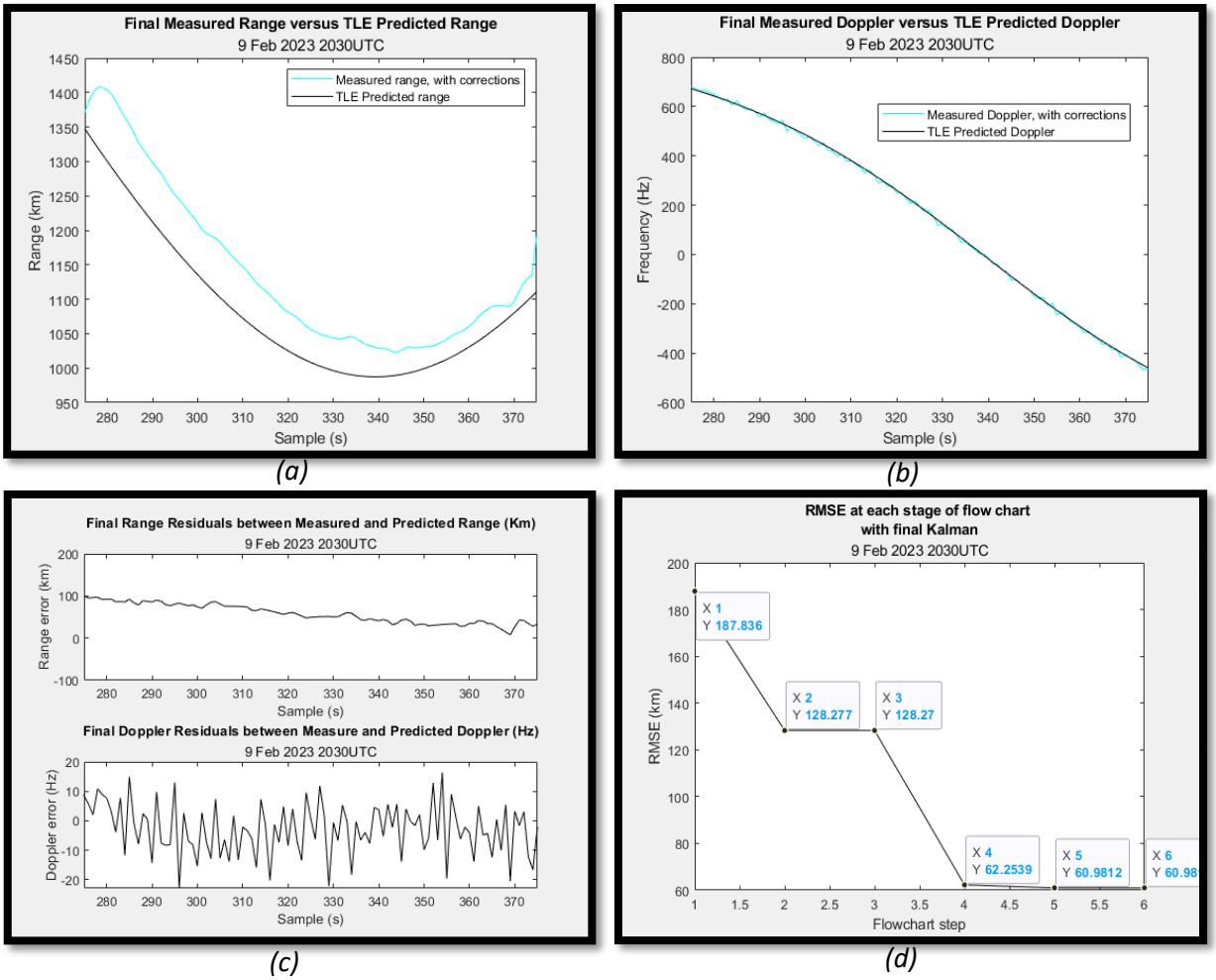

Figure 3.16 Transmission measurements 9 Feb 2023, (a) Final measured range in cyan versus TLE predicted range in black, (b) Final measured Doppler in cyan versus TLE predicted Doppler in black, (c) range and Doppler residuals against TLE predictions, (d) RMSE for each range correction step: 1. Initial Kalman Filter, 2. Matching filter error correction, 3. Tropospheric error correction, 4. Ionospheric error correction, 5. Final Kalman filter, 6. Final target range.

After all the corrections were applied during the window of visibility, the range errors can be reduced to a RMSE of 60.98 km and the Doppler frequency RMSE to 9.24 Hz. The biggest disadvantages to day time transmission, is the short observation window and much higher TEC along the propagation path, increasing the phase advances.

The following sub section will discuss the errors corrected by each step, with associated graphs for the period of visibility only.

Errors and Discussion

Figures 3.17, 3.18, and 3.20 show all the errors corrected by each step of the flow chart shown above in Figure 3.8. The first step in the flow chart is to use a Kalman Filter to smooth out some of the noise in the measurements. This proved to eliminate some of the outlier points using the measured Doppler frequencies to predict the next range position. Much higher corrections were made at the beginning and end of the transmissions when the ISS was lost to clutter and atmospheric noise, with smaller real time errors corrected throughout the visible portions of the passes.

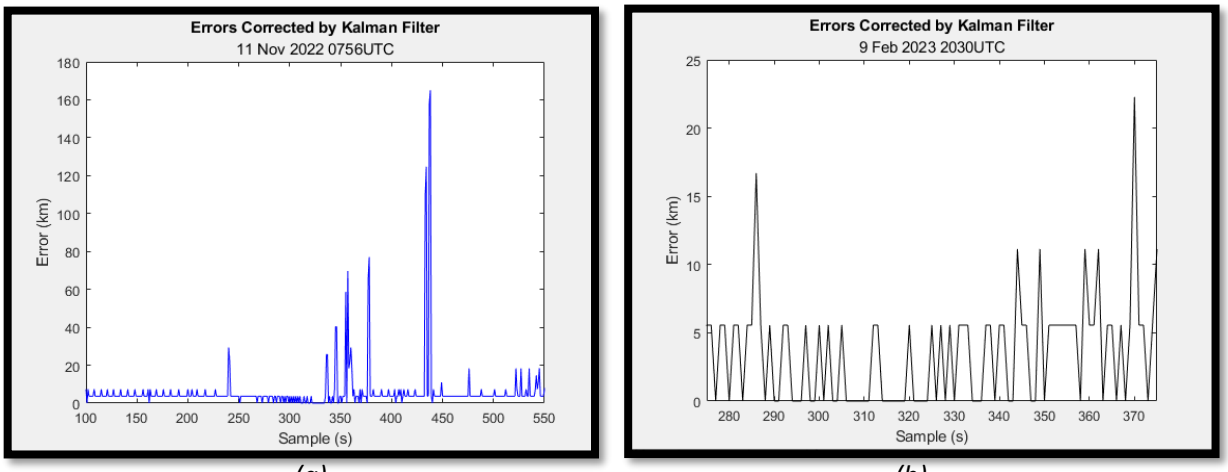

(a) (b)

Figure 3.17 Errors Corrected using initial Kalman Filter (a)11 Nov 2022, (b) 9 Feb 2023.

On average, the Kalman filter corrected 6 km during the night and 3.5 km during the day.

The second step in the flow chart was to apply the matching filter error compensation, also known as the range-Doppler coupling error. This correction proved to reduce the greatest number of errors due to the larger Doppler shift present with the fast-moving target. The range-Doppler coupling compensation saw corrections that ranged from almost -600 km to 600 km for both transmissions. Although the passes differ slightly in elevation and azimuth, the constant velocity of the ISS provides both passes with very close Doppler measurements, and therefore very similar matched filter errors, with slight differences in the middle of the pass.

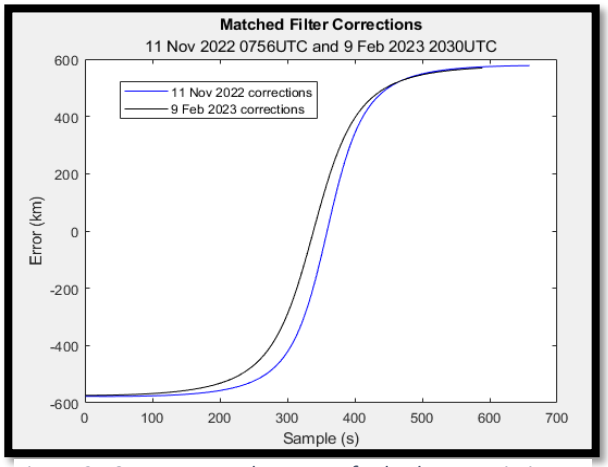

Figure 3.18 Range-Doppler Errors, for both transmission periods, in blue for the night transmission 11 Nov 22, and in black for day transmission 9 Feb 23.

Figure 3.19 shows the new estimated ranges after the matched filer corrections are applied and the associated residuals. From these, it is evident that the matched filter contributed the highest level of error for both transmissions. The night transmission, (a), is already showing near zero residuals throughout the entire pass, indicating that ionospheric corrections may not be a large contributor to measurement errors, and may be over estimated. This will be further explored when discussing the

Doppler measurements. Whereas for the day transmission, (b), there is still a large error remaining even after the matched filter correction, which can be attributed to the ionospheric effects.

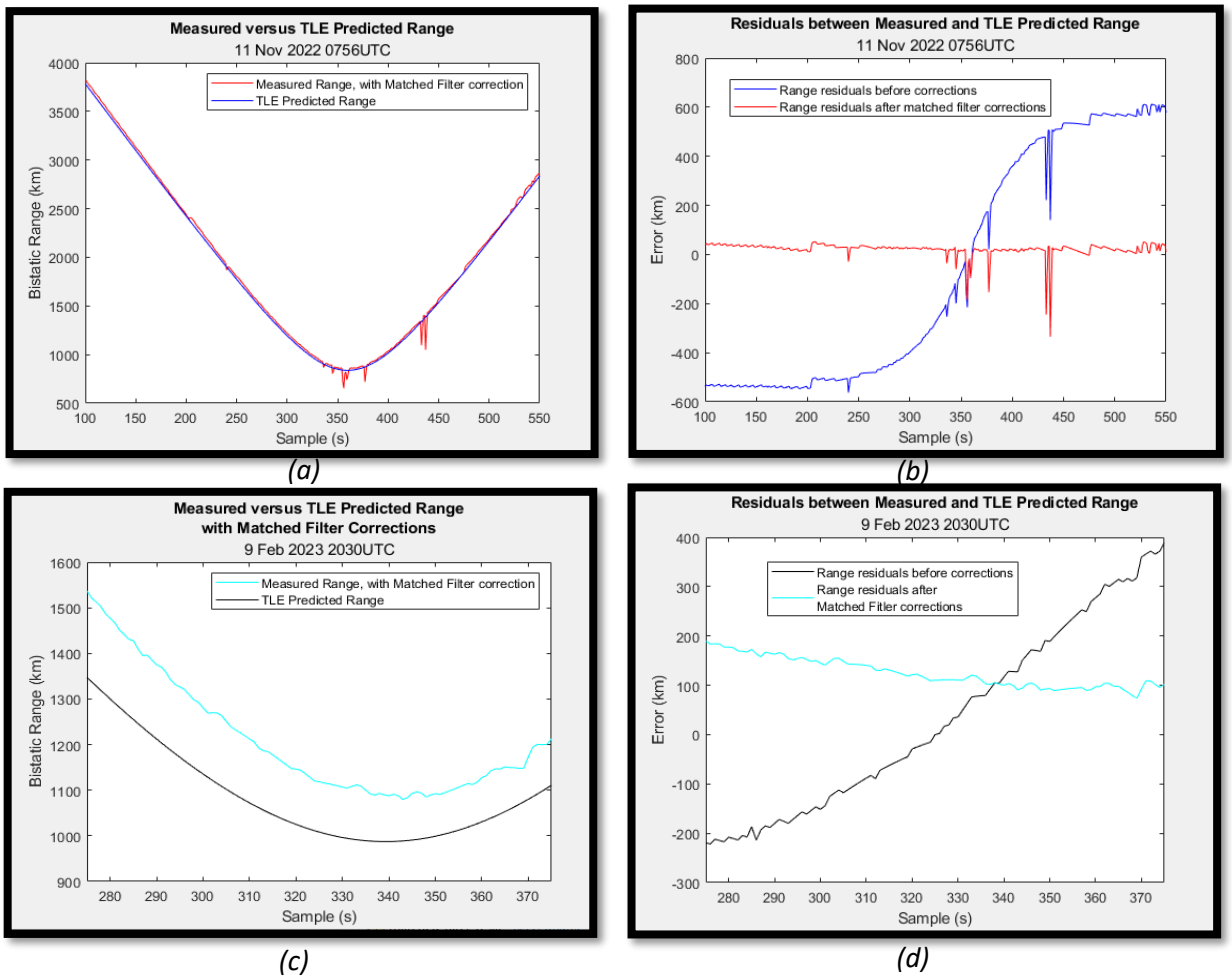

Figure 3.19 Measured and Predicted TLE ranges after matched filter corrections are applied (a) 11 Nov 2022 Measured Range after corrections in red, TLE predicted range in blue (b) 11 Nov 2022 residuals before (blue) and after (red) corrections are applied. (c) 9 Feb 2023 Measured Range after corrections in cyan, TLE predicted range in black (d) 9 Feb Nov 2022 residuals before (black) and after (cyan) corrections are applied.

The next step in the flow chart was to apply the atmospheric corrections. Using the humidity chart above in Table 3.2, the tropospheric errors were calculated and combined with the ionospheric errors to create one single atmospheric error correction step. The PHaRLAP estimated TEC along the propagation path was used to calculate the total range delay caused by the ionosphere. The ionospheric corrections varied greatly between the night transmission and the day transmission due to the large change in the TEC at these times.

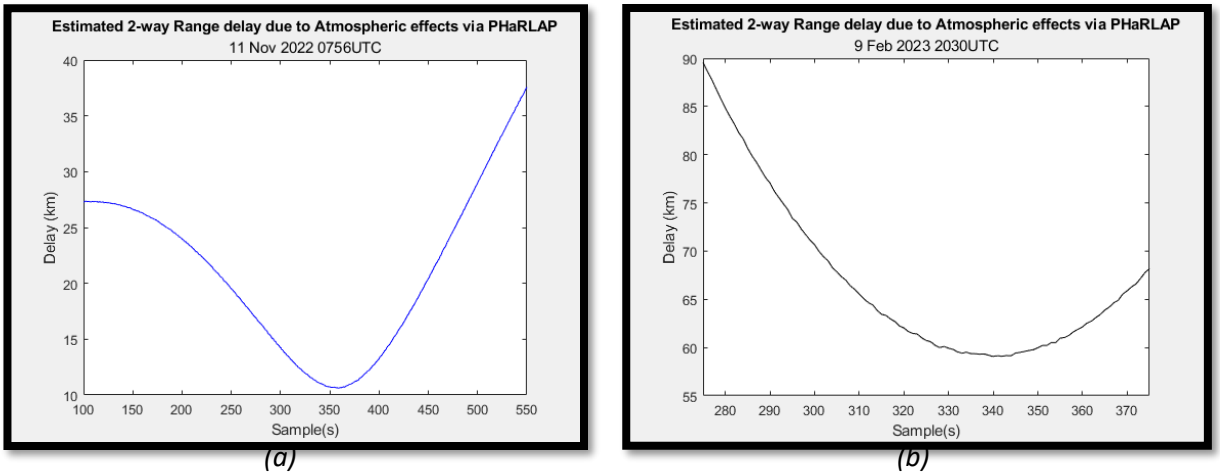

Figure 3.20 Estimated Atmospheric Errors, including Tropospheric and Ionospheric: (a) 11 Nov 2022, (b) 9 Feb 2023.

These figures highlight the effect of the solar radiation on the range delay caused by the ionosphere. The night transmission shows delays of up to 40 km, and the day transmission delays are more than double at some points, reaching 90 km. Figure 3.21 shows the residuals of the range measurements before and after the atmospheric corrections.

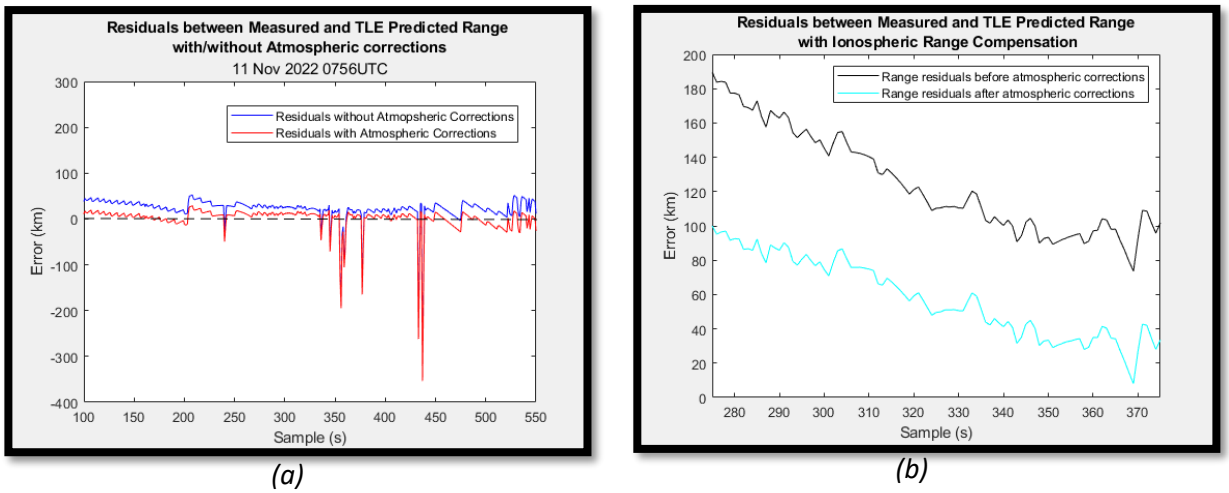

Figure 3.21 Residuals between Measured ranges and TLE predicted ranges before and after atmospheric corrections, (a) 11 Nov 2022 range residuals before corrections in blue and after correction in blue, 0 residuals is marked with black dashed-line (b) 9 Feb 2023, Range residuals before correction in black, and after in cyan.

These show that the atmosphere has a large impact during day time operations, and needs to be considered and corrected, and in this case, the effects may be under estimated. Whereas, night operations are not nearly as affected by the atmosphere, and corrections may be negligible. The RMSE for processing with and without the atmospheric corrections is shown in Figure 3.22. The range delay estimations for the night time pass show that the delay corrections provided a slight correction towards zero residuals whereas the day time measurements prove to be significantly more accurate after applying the atmospheric range delay corrections.

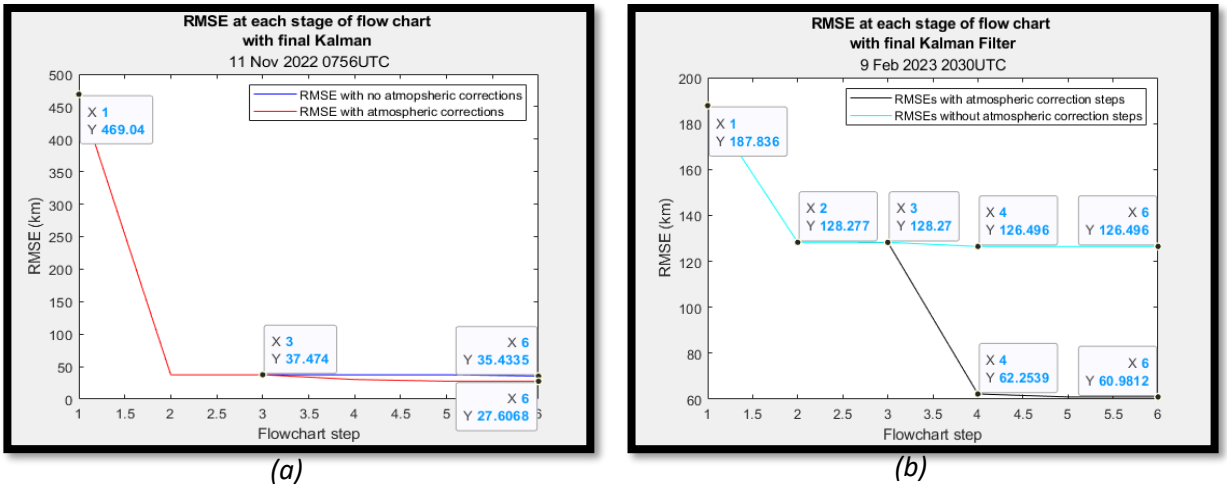

Figure 3.22 RMSE for each step of the correction flow chart with and without the atmospheric corrections applied. (a) 11 Nov 2022 RMSE without atmospheric corrections in blue and with atmospheric corrections in red. (b) 9 Feb 2023 RMSE without atmospheric corrections in cyan and with atmospheric corrections in black. Flow chart stages: 1. Initial Kalman Filter, 2. Matching filter error correction, 3. Tropospheric error correction, 4. Ionospheric error correction, 5. Final Kalman filter, 6. Final target range.

The ionospheric Doppler corrections were also applied at this stage in the processing. Figure 3.23 shows the initial Doppler residuals, (a) day and (b) night, during the visible portion of the pass and (c), (d) show the TEC estimated for both day and night. The night time Doppler residuals (a) remain very close to zero for a very large portion of the pass. This is consistent with the expected Doppler residual of a LEO satellite [7], and this indicates that the ionospheric error is very small and may not even require a correction, inline with the range measurements shown above. It also shows the expected bump around the mid point of the pass where the target would be reaching almost zero Doppler with respect to the receiver. There is a slight second bump shortly after that is not expected, however this is likely caused by a satellite maneuver. The RMSE for the uncorrected Doppler measurements during the night transmission is 5.97 Hz (85.63 m/s). On the contrary, the day time measurements (b) show a large slope in the Doppler residuals. This is likely due to the higher TEC effecting the phase advance of the carrier frequency, creating a requirement for correction. The RMSE for the uncorrected Doppler measurements during the day transmission is 33.8960 Hz (486.17 m/s). The TEC during the night reached a maximum of just over $4 \times 10^{17}\text{electrons/m}^2$, where the day time TEC is measured to be more than twice that at 9.7×10^{17} electrons/m^2.

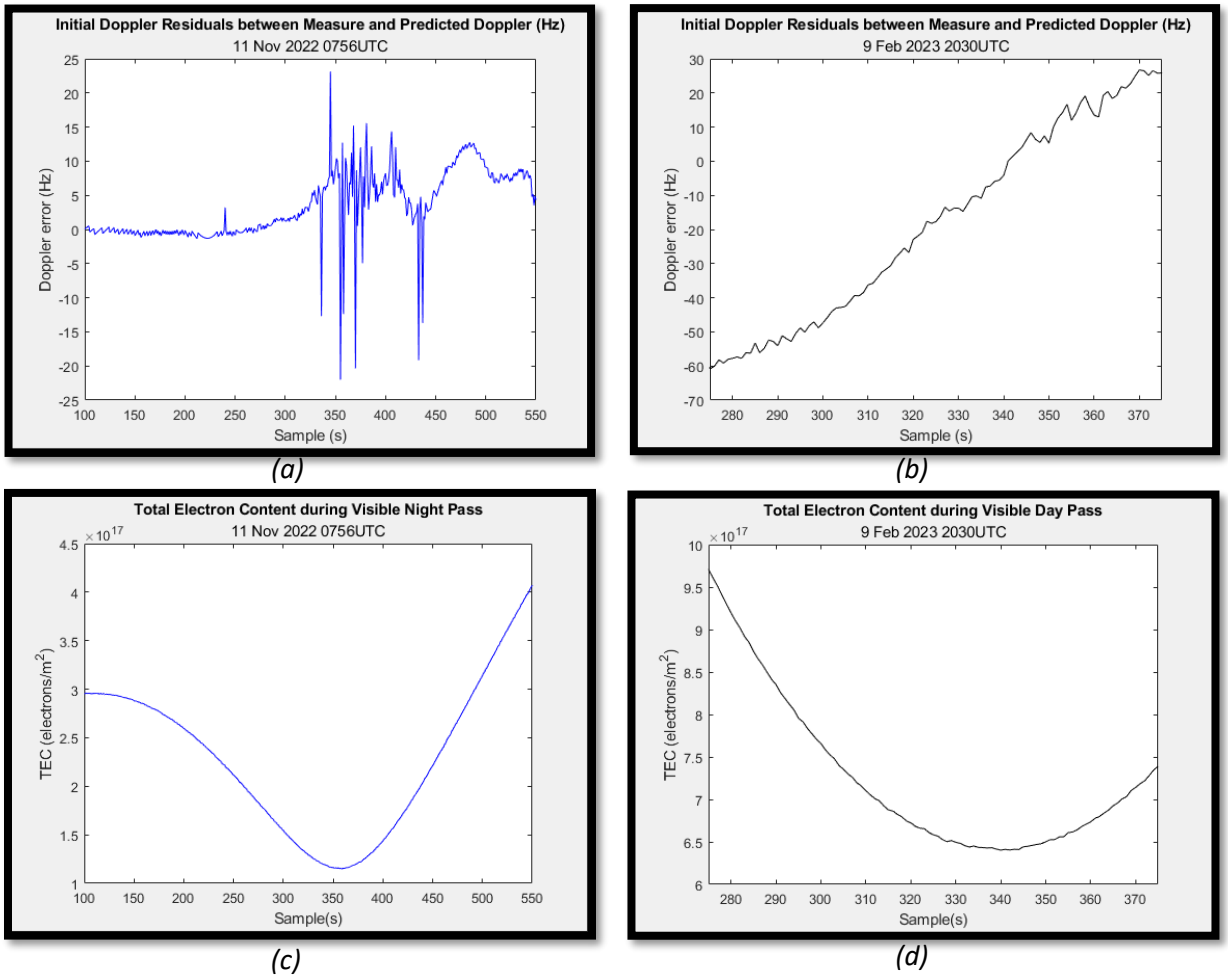

Figure 3.23 Initial Doppler Residuals (a)11 Nov 2022, (b) 9 Feb 2023 and Estimated TEC via PHaRLAP (c)11 Nov 2022, (d) 9 Feb 2023.

The ionospheric Doppler errors were calculated using the rate of change of the TEC throughout the visible portion of the pass, and then validated with a second method using the phase path error over the same period. Figure 3.24 shows the expected Doppler corrections required using both methods of correction, with a RMSE between the two errors of 0.15 Hz.

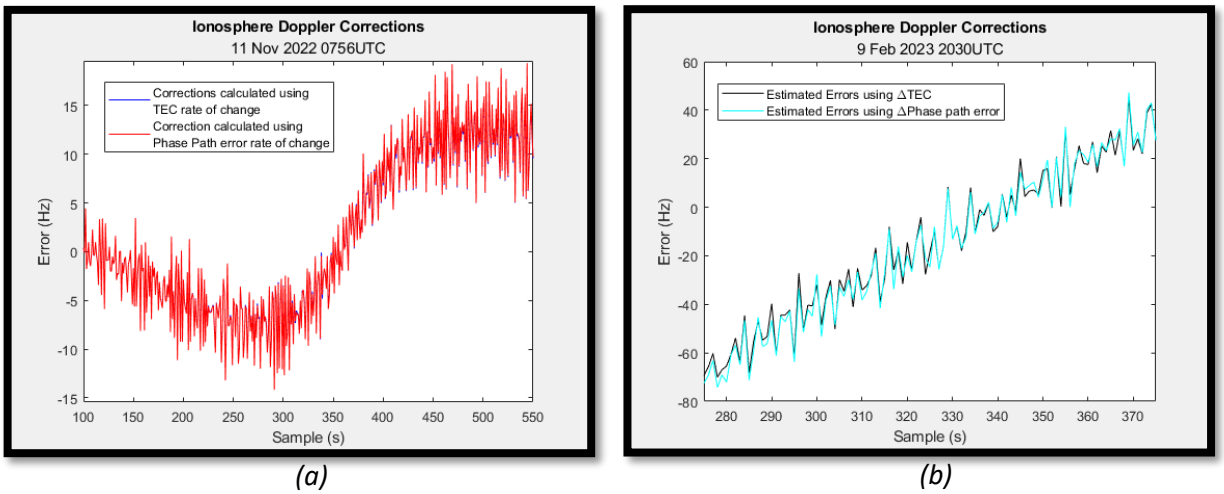

Figure 3.24 Ionospheric Doppler Corrections (a) 11 Nov 2022 calculated with TEC rate of change in blue and calculated with phase path error in blue, (b) 9 Feb 2023 calculated with TEC rate of change in black and calculated with phase path error in cyan.

As expected, the night time ionospheric Doppler corrections, ranging from -15 Hz to 15 Hz, are much lower than the day time predicted corrections, ranging from -70 Hz to 45 Hz. The ionospheric Doppler errors are correlated to the TEC that is estimated during the time of the pass, which directly effects the phase path of the RF wave, causing a phase advance in the propagated wave. With a higher TEC, a higher phase advance is expected, creating a shorter phase path and higher corrections.

Figure 3.25 shows the Doppler residuals after corrections, (a) night, (b) day. These results show that both the night and day transmission are relatively accurate with RMSEs of 6.8 Hz (97.53 m/s) and 9.24 Hz (132.53 m/s) respectively. The night time Doppler measurements actually see a slight increase in errors when compared to the original RMSE of 5.97 Hz. This indicates that the assumption of an over estimated TEC is likely valid, negating the requirement for ionospheric Doppler corrections. Therefore, the night time transmission Doppler measurements were not corrected for the final values.

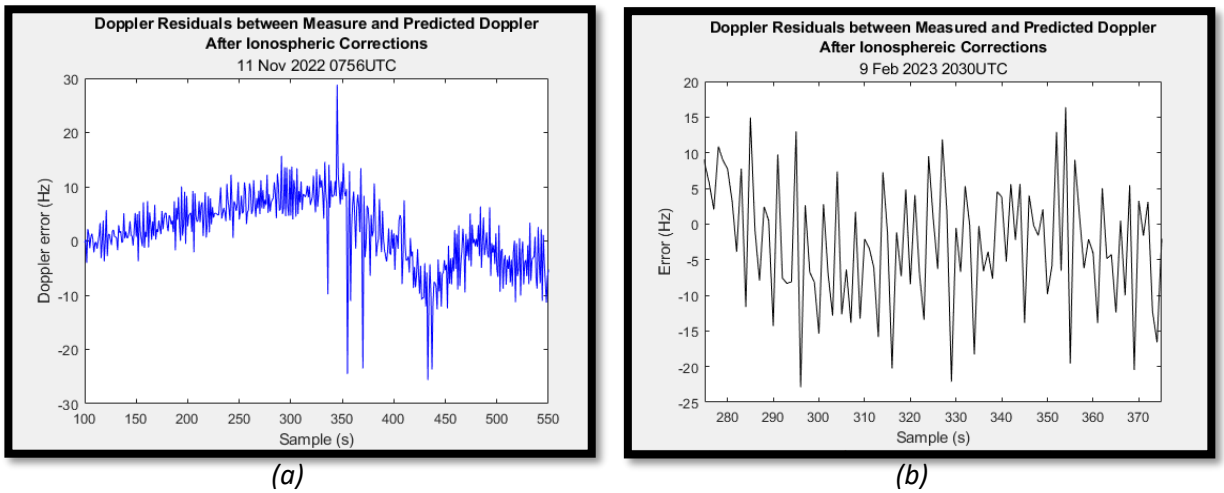

Figure 3.25 Doppler Residuals after corrections are applied (a) 11 Nov 2022, (b) 9 Feb 2023.

Figure 3.25 (a) and (b) indicate relatively accurate Doppler measurements to the TLE predicted Doppler frequencies. Since TLEs are not actual positions, and they are themselves predictions, it is

impossible to say if these Doppler measurements tend towards the actual values or away. However, since they are within a reasonable margin of error, there is potential to use these measurements for orbit determination.

Range rate estimations were calculated using the uncorrected night Doppler measurements and the corrected day Doppler measurements in Figure 3.25. These results are shown in Figure 3.26 compared against the TLE predicted range rate, and the associated residuals.

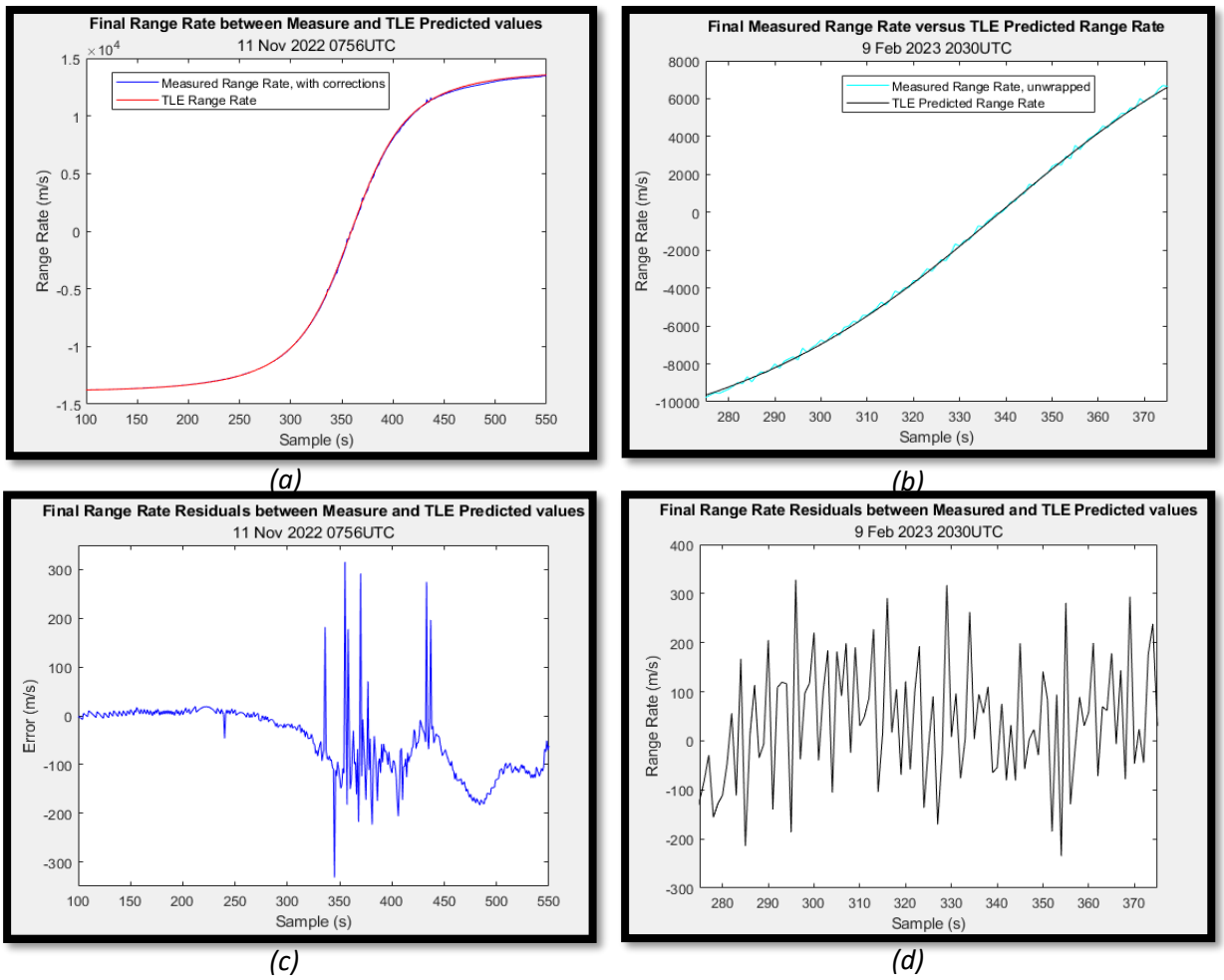

Figure 3.26 Measured versus TLE predicted Range Rate (a) 11 Nov 2022, Measured range rate in red, and TLE predicted range rate in blue, (b) 9 Feb 2023, Measured range rate in cyan and TLE predicted range rate in black, and associated residuals for each pass (c) 11 Nov 2022, (d) 9 Feb 2023.

Figure 3.26 shows the night transmission having an accuracy better than 50 m/s for most of the pass when compared to the TLE values, with an RMSE of 85 m/s. However, the day transmissions errors average between -100 m/s and 100 m/s, with an RMSE of 132.53 m/s. When using TLEs, for radial velocity errors greater than 100 m/s is not uncommon, and therefore does not eliminate HF for SDA completely.

The final measured ranges, with the lowest RSME of 27.6 km, indicates that even with the corrections applied, there is a high error still present in the measured range of the ISS when compared to the TLE. The night time data is more accurate with an RMSE of half of day time RMSE, and maintains

visibility of the ISS for a much longer time than the day time transmissions (440 s for night and only 100 s for day).

Dual Frequency Method Validation

Figure 3.27 shows the final measured ranges for 3 Nov 22. There is a higher presence of clutter and noise throughout this transmission due to the lower operating frequency of 13 MHz and a lower PRF. The ISS was visible sporadically throughout the pass, never for a long enough period for accurate signal processing. For the majority of the pass, the ISS was lost to clutter and noise or was difficult to differentiate from clutter. The transmission was rotating between three pulses of different frequencies, reducing the PRF to 16 Hz. The frequency of operation used for this part of the experiment was much lower than the other portion of the research, only 13 MHz, which was not sufficient to accurately locate and track the ISS. The data that was collect did not allow for accurate processing techniques, therefore this portion of the research was not able to be completed.

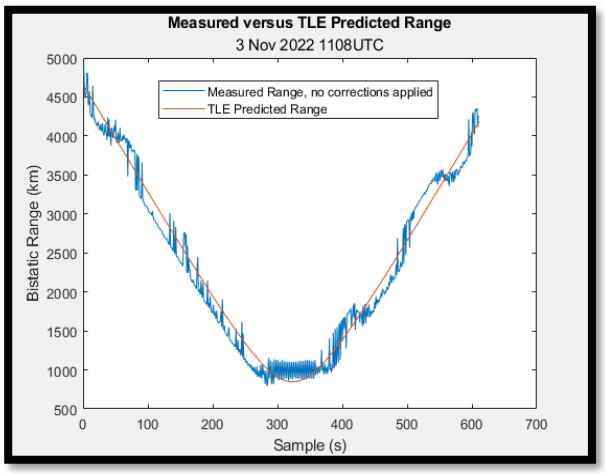

Figure 3.27 Final range measurements for 3 Nov 2022, measured ranges in blue and TLE predicted in orange.

3.3.2 – Validation

Truth data was requested from NASA to be used as a means to validate the HF estimation for SDA. However, no truth data was ever provided. Therefore, since the accuracy of TLEs is known, it can be assumed that if the range data is not within 2 km of the TLE, it is likely less accurate than the TLE and not a suitable means for SDA. The most recent TLE at time of transmission was used for each signal processing, to ensure that the TLE error remained within 1 km in position and 1 m/s in velocity. The range rates measured throughout this experiment are radial velocities, and TLE errors of over 100 m/s are not uncommon [7].

Chapter 4

Findings and Concluding Remarks

4.1 – Analysis of Results

Based on the results shown above in section 3.3, it has been shown that it is possible to locate and track the ISS to an accuracy of 27.6 km and between ± 50 m/s in radial velocity at specific points in the passes. Due to the lack of truth data from NASA, the relative accuracy with respect to the actual position cannot be confirmed. Since the positional error has more than 2 km variation from the TLE, it can be determined that the range measurements are not accurate enough to rely on HF propagation for SDA. However, there are other processing techniques and areas of research that could potentially be applied to increase the accuracy of these measurements.

Although the range measurements did not have enough accuracy to prove useful for decreasing SDA error, the Doppler frequency and range rate measurements proved relatively accurate after corrections and ambiguities were removed. Some epochs measured a range rate residual up to 200 m/s when compared to TLEs predicted range rate, however for the majority of the night time pass measured range rate residuals of less than 50 m/s. Two-way radial velocity errors of at least 10m/s are typically measured for LEO satellites. These results could be used in future research for orbit determination.

The night Doppler frequencies originally measured a RMSE of 5.96 Hz, and after correction the RMSE increased to 6.8 Hz. This indicates that the ionospheric effects were over estimated using the PHaRLAP software for the night time. The day time Doppler showed a much larger variation, with measured frequencies of a RMSE of 33.89 Hz and a corrected RMSE of 9.24 Hz. This indicates the day time data required corrections for range and Doppler measurements in order to be remotely accurate, and may have even been underestimated.

The night transmission located the ISS for the longest period of time due to the lower level of electrons found in the ionosphere, however the ISS was still located for a portion of the day pass, when the ISS was closest to the receiver, and received power is the highest. The higher frequency of 20 MHz proved to be more effective than the lower 13 MHz that was initially used. Using a lower frequency of 13 MHz proved ineffective for LoS operations.

4.2 – Future Research to be Conducted

The results show that HF is not an ideal choice for SDA, however there is an indication of potential in the Doppler measurements for accurate orbit determination. There are other areas of research that could further develop this research to increase the potential of HF for SDA.

Frequency and Shift Selections

The frequency selected for the dual frequency estimation was 13 MHz, which is a relatively low frequency when attempting LoS communications. This frequency was selected solely due to a lack of licence to transmit at 20 MHz available at the time. If this experiment were to be repeated, a higher frequency choice would provide lower unwanted clutter, and potentially allow for transmission at lower elevations.

The frequency shifts that were selected were arbitrary and chosen without consideration to the PRF being used. Other than the 66.7 Hz shift, the frequency shifts aligned with multiples of the PRF causing the pulses to overlap. It is recommended that different frequency shifts be used for any re-creation of this experiment.

Signal Processing

There is potential to use HF for real-time TEC measurements if there is a higher level of signal processing applied to the measured data. An area that could be furthered explored would be the use of

discrete wavelet packet analysis for deconstructing the dual-frequency signal to measure more accurate TEC as well as for clutter suppression.

The wavelet package analysis realizes the signal in both frequency and time domain vice one or the other as seen in more traditional signal processing such as the FFT. The wavelet transform is a method used in order to analyze how a spectrum of a signal evolves with time by analyzing a signal at different frequencies with different resolutions. Through this method, it may be possible to separate the pulses with higher resolution in order to more accurately measure the phase shifts. This would allow for more accurate TEC estimations and validation of the dual frequency method discussed in ref [18].

TEC Estimations

The software that was used for TEC estimation used the IRI 2016 model, as mentioned in section 3.3.2. This model uses prediction software to estimate the expected behaviours of the ionosphere at selected times and dates. For more accuracy, a real time measurement of the ionosphere would provide better TEC values that would calculate more accurate atmospheric correction requirements, avoiding the overestimation that was seen in the night-time data.

Orbit Determination

Orbit determination was not completed for this research. However, with the Doppler and range rate measurements it could be possible to estimate a relatively accurate orbit for the ISS. This is an area that should be further developed. Using TLEs and correcting with the measured Doppler frequency and range rate, the orbital parameters could be estimated using a least squares estimator.

Antenna Configuration and Element Selection

The antenna configuration and element choice created a higher level of noise and mutual coupling for the type of propagation being performed. Future research could develop better array elements or configurations that would be ideal for LoS transmission vice the monopoles that were selected for null steering and Arctic operations. As shown in Figure 3.5, there is an elevation limitation above 70 degrees. This will impede the array's ability to follow the ISS/target for the entire pass, incurring the requirement for some kind of predictive processing to fill the gaps. More directional elements should be considered for future research, such as log-periodic or Yagi-Uda elements.

The configuration should also be considered when designing the array for SDA specific operations. Although a square-planar array allows for steering in both azimuth and elevation which is ideal for the primary purpose of Arctic operations, there could be benefits to trying different shapes:

1. Planar circular array;
2. Linear L shaped; or
3. Linear x shaped.

There are many other elements and configurations that could be considered to create an array more conducive to SDA operations.

4.3 – Concluding Remarks

Conclusion

In conclusion, the current OTHR at DRDC is not ideal to conduct SDA while using HF frequencies. The lowest measured RMSE for range across all passes was 27.6 km. The Doppler and range rate measures show potential for orbit determination with residuals as low as 40 m/s at some points for the night transmissions. Although no truth data was available to validate the accuracy of the ISS position, the relative accuracy compared to the known accuracy of the TLE indicates that HF transmissions were

not able to reduce the SDA range errors to a better state than already accessible. There are areas of further research that could be of interest to revisit this concept, and potentially prove fruitful, such as better frequency selection, different signal processing methods, and antenna design. The Doppler measurements proved to be accurate enough to pursue further research into orbit determination.

Acknowledgements

This section is reserved to acknowledge the contributions of several outside sources that were used to produce the research presented in this document.

Thesis Supervisors

Dr. Simon Henault and Dr. Antar Yahia were the two thesis supervisors for this experiment. Dr. Simon Henault conducted the physical experiments and collected the data using the OTHR in Ottawa. The background theory discussed in this paper is primarily based on Dr. Simon Henault's previous work and designing process of the OTHR system. Indicated figures were provided by Dr. Henault.

Dr. Antar acted as the primary thesis supervisor, conducting required admin and guidance throughout the entire process. He provided basic radar principal theories and access to a wide variety of resources that were referenced within this document.

Tropospheric Errors

The tropospheric errors were estimated using a MATLAB program developed by Dr. Malek Karaim. The MATLAB routine was provided with permission to utilize in this research. Dr. Karaim also aided in the design of the Kalman Filters.

PHaRLAP

Some of the results published in this paper were obtained using the HF propagation toolbox, PHaRLAP, created by Dr Manuel Cervera, Defence Science and Technology Group, Australia (manuel.cervera@dsto.defence.gov.au). This toolbox is available by request from its author.

References

[1] O. C. RCS, "Station Results - Historical Data," Government of Canada, 31 Jan 2023. [Online]. Available: https://climate.weather.gc.ca/historical_data/search_historic_data_stations_e.html?searchType=stnName&timeframe=1&txtStationName=ottawa&searchMethod=contains&optLimit=yearRange&StartYear=2022&EndYear=2023&Year=2023&Month=3&Day=19&selRowPerPage=25. [Accessed 20 Mar 2023].

[2] "Canadian Space Agency," Government of Canada, 08 12 2021. [Online]. Available: https://www.asc-csa.gc.ca/eng/default.asp . [Accessed 9 03 2022].

[3] J. Ramsauer, "Ecology for the Masses," Radar vs. Optical: Optimising Satellite use in land cover classification, 27 May 2020. [Online]. Available: https://ecologyforthemasses.com/2020/05/27/radar-vs-optical-optimising-satellite-use-in-land-cover-classification/#:~:text=Optical%20satellite%20imagery%20is%20a,in%20almost%20all%20weather%20conditions.. [Accessed 08 March 2022].

[4] C. Livingstone, "Radar Systems for Monitoring Objects in Geosynchronous Orbit," Defence Research and Development Canada, Ottawa, 2013.

[5] J.-F. Guimond and S. Henault, "LEO Doppler Curves Satellite Tracking and Characterization," Defence Research and Devleopment Canada, Ottawa, 2020.

[6] N. Chahat, CubeSat antenna design, Wiley, 2021.

[7] S. Henault and J.-F. Guimond, "Orbit Estimation Using Passive Radio Frequency Observations," Defence Research and Development Canada, Ottawa, 2021.

[8] F. R. Hoots and R. L. Roehrich, "Project Space Track," Aerospace Defense Command United Sates Air Force, 1980.

[9] U. S. Force, "Space-Track.org," Space-Track, [Online]. Available: https://www.space-track.org/documentation#/sgp4. [Accessed 16 Sept 2022].

[10] unknown, "N2YO.com," [Online]. Available: https://www.n2yo.com/satellite/?s=25544. [Accessed 6 July 2022].

[11] S. Caldwell, "Communications," in *SOA*, National Aeronautics and Space Administration, 2021, pp. 232-252.

[12] J. Keeler and R. J. Serafin, "HF Over the Horizon Radar," in *Radar Handbook*, 3rd ed., M. Skolnik, Ed., The McGraw-Hill Companies, 2008, pp. 20.1-20.70.

[13] B. Dunbar, "Earth's Atmospheric Layers," National Aeronautics and Space Administration, 22 January 2013. [Online]. Available:

https://www.nasa.gov/mission_pages/sunearth/science/atmosphere-layers2.html. [Accessed 19 June 2023].

[14] E. S. Agency, "Navipedia," European Space Agency, 13 Jan 2013. [Online]. Available: https://gssc.esa.int/navipedia/index.php/Tropospheric_Delay#:~:text=Troposphere%20is%20the%20atmospheric%20layer%20placed%20between%20earth%27s,the%20signal%20traveling%20from%20the%20satellite%20to%20receiver.. [Accessed 17 March 2023].

[15] P. Rohan, Introduction to Electromagnetic Wave Propagation, London: Artech House Publishers; Illustrated edition, 1991.

[16] M. I. Skolnik, Radar Handbook, The McGraw-Hill Companies, 2008.

[17] A. G. B. o. Meteorology, "Australian Space Weather Forecasting Centre," Commonwealth of Australia, 2022. [Online]. Available: https://www.sws.bom.gov.au/HF_Systems/6/5. [Accessed 05 10 2022].

[18] J.-T. Lyu and C. Zhou, "A Technique for Real-Time Ionospheric Ranging Error Correction Based on Radar Dual-Frequency Detection," *Radio Science*, no. 52, pp. 1604-1614, 2017.

[19] R. A. Halliwell, Whistlers and Related Ionospheric Phenomena (2nd Edition), Mineola: Dover, 2006.

[20] M. A. Richards, J. A. Scheer and W. A. Holm, "Ambiguity Functions," in *Principles of Modern Radar*, Raleigh, SciTech Publishing, 2010, pp. 800-808.

[21] J. A. Klobuchar, "Ionospheric Effects on Earth-Space Propagation," Air Force Geophysics Laboratory, Bedford, 1983.

[22] F. Wild, "What is the International Space Station?," NASA, 30 October 2020. [Online]. Available: https://www.nasa.gov/audience/forstudents/5-8/features/nasa-knows/what-is-the-iss-58.html. [Accessed 7 July 2022].

[23] A. F. Purkhauser, "On the Use of Doppler Measurements for Dynamic Orbit Computation Case Study: GRAIL," Graz University of Technology, Styria, 2015.

[24] R. G. Brown and P. Y. Hwang, Introduction to Random Signals and Applied Kalman Filtering, 3rd ed., John Wiley & Sons , 1997.

[25] M. Cervera, "Australian Government Defence Science and Technology Group," Astralian Government, [Online]. Available: https://www.dst.defence.gov.au/our-technologies/pharlap-provision-high-frequency-raytracing-laboratory-propagation-studies. [Accessed 10 May 2022].

[26] Collins English Dictionary, "Dictionary.com," HarperCollins, New York City, 2012.

[27] M. I. Skolnik, "Theoretical Accuracy of Radar Measurements," in *Introduction to Radar Systems Third Edition*, New-Delhi, Tata McGraw-Hill Publishing Company Limited, 2001, pp. 317-331.

[28] G. Frazer, D. Meehan and G. Warne, "Decametric measurements of the ISS using an experimental HF line-of-sight radar," in *International Conference on Radar*, 2013.

[29] S. Thorsteinson, *Space Surveillance from a Microsatellite,* Division of Graduate Studies of the Royal Military College of Canada, 2017.

[30] Government of Canada, "NEOSSat: observing asteroids, space debris and exoplanets," Government of Canada, 24 February 2023. [Online]. Available: https://www.asc-csa.gc.ca/eng/satellites/neossat/. [Accessed 27 June 2023].

[31] R. Leitch, "Sapphire: A Small Satellite System for the Surveillance of Space," in *AIAA/USU Conference on Small Satellites*, 2010.

[32] J.-F. Guimond, S. Henault and K. Levis, "One-way Doppler and Interferometry: Space Domain Awareness," Defence Research and Development Canada, Ottawa, 2021.

[33] S. Henault and R. J. Riddolls, "Two-dimensional transmit arrays for polar over-the-horizon radar," *IET Radar Sonar Navigation*, vol. 15, pp. 1165-1172, 2021.

[34] C. A. Balanis, Antenna Theory Analysis and Design, Hoboken: John Wiley & Sons, Inc., 2016.

[35] Altair Engineering, "7.0 FEKO Example Guide," EM Software & Systems-S.A. (Pty) Ltd, Stellenbosch, 2014.

[36] Z. Guo, Y. Yao, J. Kong, G. Chen, C. Zhou, Q. Zhang, L. Shan and C. Liu, "Accuracy Analysis of International Reference Ionosphere 2016 and NeQuick2 in the Antarctic," *Sensors*, vol. 21, no. 4, 23 Feb 2021.

[37] N. Hall, "Mach Number," NASA, 2021. [Online]. Available: https://www.grc.nasa.gov/www/k-12/airplane/mach.html. [Accessed 6 10 2022].

[38] C. Q. Choi and A. Harvey, "Asteroids: Fun facts and information about these space rocks," Space.com, 22 November 2021. [Online]. Available: https://www.space.com/51-asteroids-formation-discovery-and-exploration.html. [Accessed March 2022].

[39] S. Clark, "Canadian Asteroid-hunting Satellite to Launch Monday," 23 Feb 2013. [Online]. Available: https://spaceflightnow.com/news/n1302/23neossat/. [Accessed 08 Mar 2022].

[40] M. A. Cervera and L. Pederick, "Semiempirical Model for Ionospheric Absorption based on the NRLMSISE-00 atmospheric model," *Radio Science*, no. 49, pp. 81-93, 2014.

[41] M. Manning, "Passive radar target tracking with a Kalman filter," Dopplerfish.com, 9 May 2020. [Online]. Available: https://dopplerfish.com/passive-radar-target-tracking/. [Accessed 20 March 2023].